

Exploring computational techniques for simulating residual stresses for thin wall multi-joint hexagon configurations for a laser directed energy deposition process

Bitá Mohajemia (✉ bita.mohajemia@gmail.com)

University of Windsor Faculty of Engineering <https://orcid.org/0000-0001-7119-2490>

Jill Urbanic

Research Article

Keywords: Directed energy deposition, laser cladding, FEM, numerical analyses, simulations, computational techniques, thin wall, residual stress

Posted Date: June 1st, 2022

DOI: <https://doi.org/10.21203/rs.3.rs-1662554/v1>

License:  This work is licensed under a Creative Commons Attribution 4.0 International License.

[Read Full License](#)

Exploring computational techniques for simulating residual stresses for thin wall multi-joint hexagon configurations for a laser directed energy deposition process

Bitra Mohajernia¹ mohajerb@uwindsor.ca, Jill Urbanic¹ jurbanic@uwindsor.ca

1: Department of Mechanical, Automotive and Materials Engineering, University of Windsor, Sunset Ave, Windsor N9B 3P4, Ontario, Canada

Corresponding author: Bitra Mohajernia, mohajerb@uwindsor.ca

Abstract:

Laser cladding is a directed energy deposition process, and can lead to high residual stresses, which can compromise the quality of the specimen. As a result, it is crucial to accurately predict and investigate the residual stress distribution in clad parts and understand the mechanism of formation. In this study a thermo-mechanical metallurgical simulation model of the laser cladding process was developed for three different path strategies with respect to the deposition sequence and direction for a single layer, thin wall hexagon with inner junctions to investigate the formation of residual stress. The study was extended to a five layer scenario. A comparison of two types of computational techniques, the detailed transient approach and the imposed thermal cycle approach, was performed. Consistent results were observed when comparing the resultant stress patterns. Subsequently, the imposed thermal cycle method was applied for the five layer models. A preheat scenario is explored. This reduced the computational cost to great extent, but the stress patterns were not similar. The differences between the implemented computational techniques are described as well as the advantages and disadvantages of each. Knowledge obtained from these case studies provides a foundation for efficient and rapid optimization of laser cladding processes, with the aim of minimizing residual stress in both simple and complex laser cladding structures. **Keywords:** Directed energy deposition, laser cladding, FEM; numerical analyses; simulations; computational techniques; thin wall; residual stress

1 Introduction

Directed energy deposition is one of the most important additive manufacturing (AM) processes for making, repairing, and modifying geometrically complex metallic components, and could significantly reduce product design-to-market times [1], [2]. The parts built by a DED technique such as laser cladding are exposed to repeated heating and cooling cycles during manufacturing. Residual stress forms during these rapid heating and cooling cycles.

Residual stress in additively manufactured metallic parts is a disadvantageous factor that hinders its wide application. Cracking and distortion will occur when the thermal stress is too high. As the sizes of manufactured part increase, the part become subject to greater distortion and stress. Especially for thin-wall parts, the final geometry is often significantly different from the original design [3]. Therefore, residual stress and distortion characteristics must be investigated, and control mitigation strategies proposed.

The highly coupled thermo-mechanical behavior of the materials, microstructure evolution, and fluid flow inside molten pools makes it difficult to predict residual stresses accurately [4]. Finite element analysis (FEA) is increasingly used to predict the thermo-mechanical behavior of the laser cladded parts including thermal stresses and distortion. Li et al. [5] developed an FE model for predicting the thermal cycle and residual stresses of an inclined thin wall. Some researchers have studied the thermal cycle and residual stress of a circular part [6]–[8]. This literature focuses on modeling and prediction; however, few of them are concerned with optimization strategies in regard to simulation techniques or path planning.

The tool path strategy and its effects on residual stress has been studied by many researchers. Zhao et al. [9] established an FE model of a ten-layer wall and realized that the deposition direction strongly impacts the resulting stress and strain. Deposition in a reciprocating direction performed better than deposition in the same direction. Somashekara et al. [10] developed an FE model of parts with three different deposition paths (raster, a spiral-in and spiral-out) in wire and arc additive manufacturing. The raster patterns had the least residual stress of the three designs. Wu et al [11], investigated the residual stress in the cubic rectangle made by printing of titanium and nickel alloys using wire arc additive manufacturing and concluded that the residual stresses in the short deposition raster pattern were smaller than those in the long deposition raster and spiral-in pattern. The finite element method was used by Sun et al. [12] to investigate the temperature field and stress field of cuboids deposited by five different patterns: zig-zag, raster, alternate-line, in-out spiral, out-in spiral, and an S-pattern. The S-pattern had the lowest residual stress, according to the results. However, Mirazimzadeh et al. showed that there is coupling between the tool path and the geometry; consequently, a solution for one configuration cannot be assumed to be transferrable to another configuration [13]. The previous studies focused on prediction of residual stress in simple and straightforward geometrical parts. They rarely have more complex geometrical features or a thin walled configuration with junction structures, which have significant importance for practical industrial production.

The use of numerical models enables cost-effective prediction of thermal effects, avoiding the time and cost of experiments, and data can be extracted from the complete model. There are two perspectives being studied in this research for analyzing and solving the laser cladding process simulations. In the first approach a detailed and often partial solution of some of the effects of the laser cladding process, consisting of the molten pool size and shape, heat affected zone and in general the metallurgical and mechanical modifications in the cladded joint is investigated [14], [15]. A detailed description of the solution including distribution of temperatures, hardness, the metallurgical phases, stresses, and deformations is the result of this type of analysis.

The transient models implemented in the above-mentioned literature is not an effective approach to simulate large-scale manufacturing processes. Due to the transient nature of the analysis, the simulation running time is relatively high. Consequently, intelligent approaches should be used to reduce modeling complexity without compromising the accuracy of the results.

The second approach is the application of numerical analysis to large and complex part. However due to the complexity of the problem simplifications should be applied, which to some extent decrease the accuracy of the calculations and results [16][17][18][19]. Although this is a

disadvantage, it allows conducting analyses that in the first approach are impractical to perform [15]. Min Zhu et al.[20] investigate the influence of welding sequence on evolution of residual stress in bimetallic clad plate butt-welded joint using the imposed thermal cycle method. They concluded that the longitudinal residual stress evolution is greatly influenced by the welding sequence. Different welding sequences do not affect the peak value of the surface residual stress on the flyer plate for bimetallic clad plate joints. Wang et al. [21] studied the residual stress formation in multi-layer welding T-joints using the imposed thermal cycle method and validated their findings with experimental measurements using X-ray diffraction method. Although many researchers have studied various FEA approaches for a variety of materials, there are limited residual stress studies on more complex geometries with a system of joints and junctions that are typical for functional components.

The long-term goal of this research is to develop optimal process planning strategies to ensure that the built geometry meets the requirements while minimizing the residual stresses. In this research, an investigation is carried out on the influence of the bead deposition sequence and directions on the residual stress formation in a complex thin-walled hexagon with several interior junctions. This shape is symmetric and contains three and four joint junctions. An optimized computational technique is implemented, and its performance is compared to the detailed transient heat source approach method. The optimized technique is utilized to investigate the residual stress for a multilayer hexagon shape structure, which is extremely time consuming using transient approach.

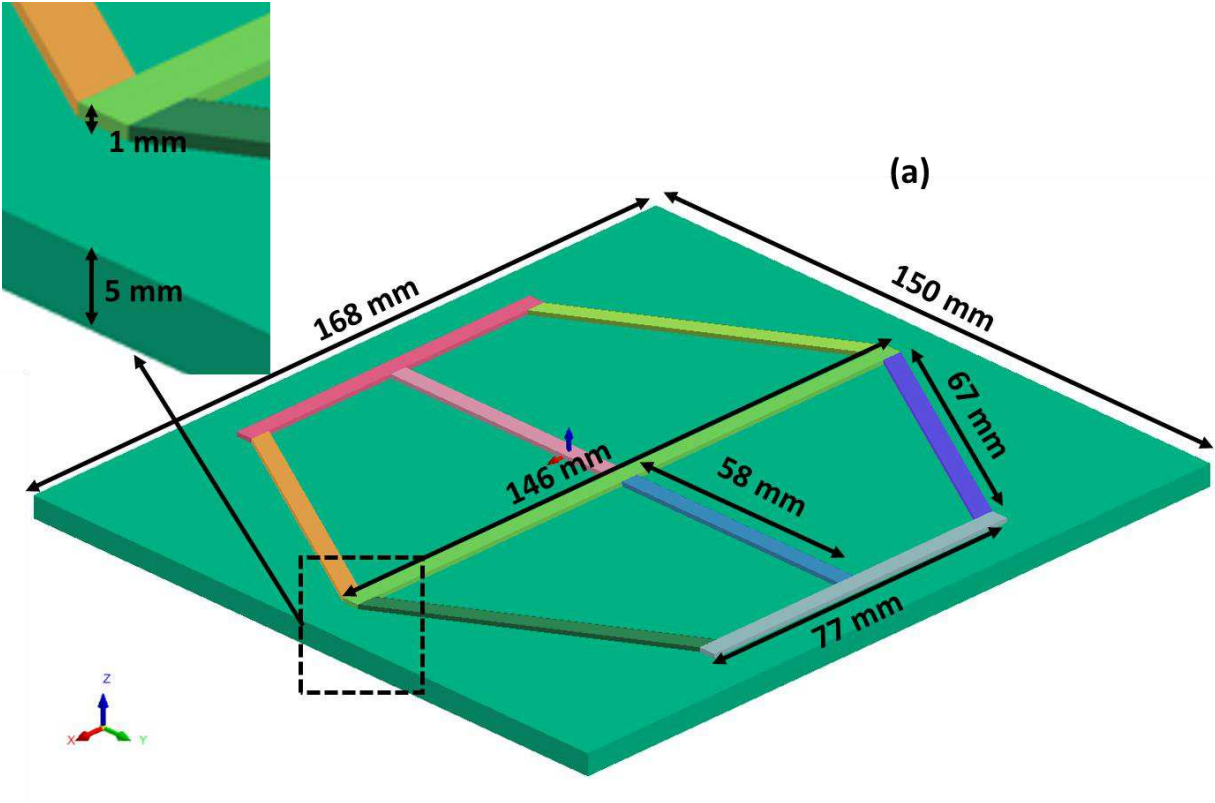
2 Research methodology

In this work the thermo-mechanical model has been developed using one and five layer hexagon CAD models as representative case studies. For the thermal analysis portion, the heat source parameters, boundary conditions and temperature dependent material properties were assigned to the meshed model. The transient temperature fields were calculated, and an optimized estimation of temperature fields is proposed and at last the mechanical calculations using the thermal results and applying mechanical boundary conditions. The results are compared showing the merits of this approach and the issues to be resolved for large, intricate thin wall components.

2.1 Development of thermo-mechanical model

In Figure 1(a) the geometric size of the thin-wall hexagon shape part and its substrate are presented. Figure 1(b) shows the 5 layer hexagon model with similar dimensions and sizes while the number deposited beads has increased. The mechanical boundary conditions were applied to the bottom surface of the substrate during the calculation to avoid rigid body motion. It is assumed that the substrate is located on a table and this condition is called the unclamped condition. The details of the applied boundary conditions are shown by the arrows in Figure 2. The geometry was meshed using eight noded brick elements. After performing the mesh sensitive analysis, the average element size in the bead regions and closer to the heat source is $0.5 \times 0.5 \times 0.5$ mm. A relatively coarse mesh is assigned in the remaining part. The total number of elements for the one-layer hexagon and the five layers hexagon are 15363 and 30788 respectively. Figure 3 shows the temperature-dependent material properties of the AISI 1018 substrate and P420 stainless steel beads.

Figure 4 presents the three deposition sequences and the directions considered for the thin wall one-layer hexagon. The results indicate that the number 3 path sequence results in lower tensile residual stress. Therefore, it has been selected and investigated for the five layers deposition case studies. The scanning direction is consistent for all five layers of the multi-layer case study. The simulations for both patterns were conducted under the same process parameters and efficiency. During the laser cladding process, three different heat transfer phenomena occur, which are: conduction, convection and radiation. Figure 5 shows the heat input from the laser and the heat loss due to convection and radiation as well as conduction into the substrate. A 600 second delay is considered for the cooling stage to ensure that the model cools down to room temperature (20°C) naturally.



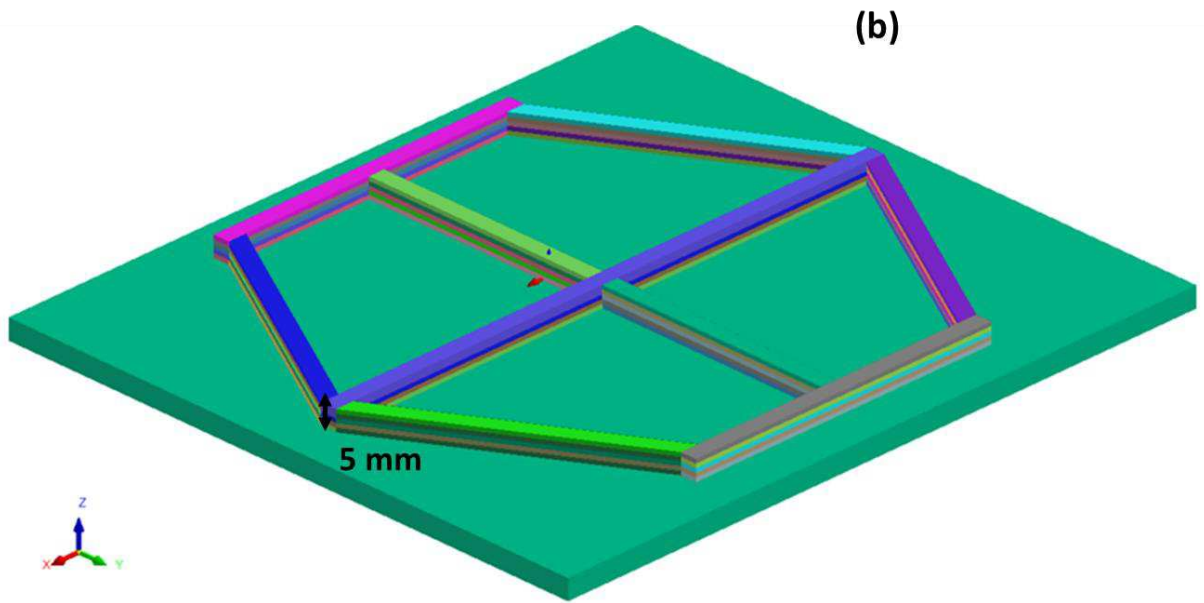


Figure 1. Geometrical size of the hexagon for (a) the one-layer scenario, and (b) the five-layer scenario

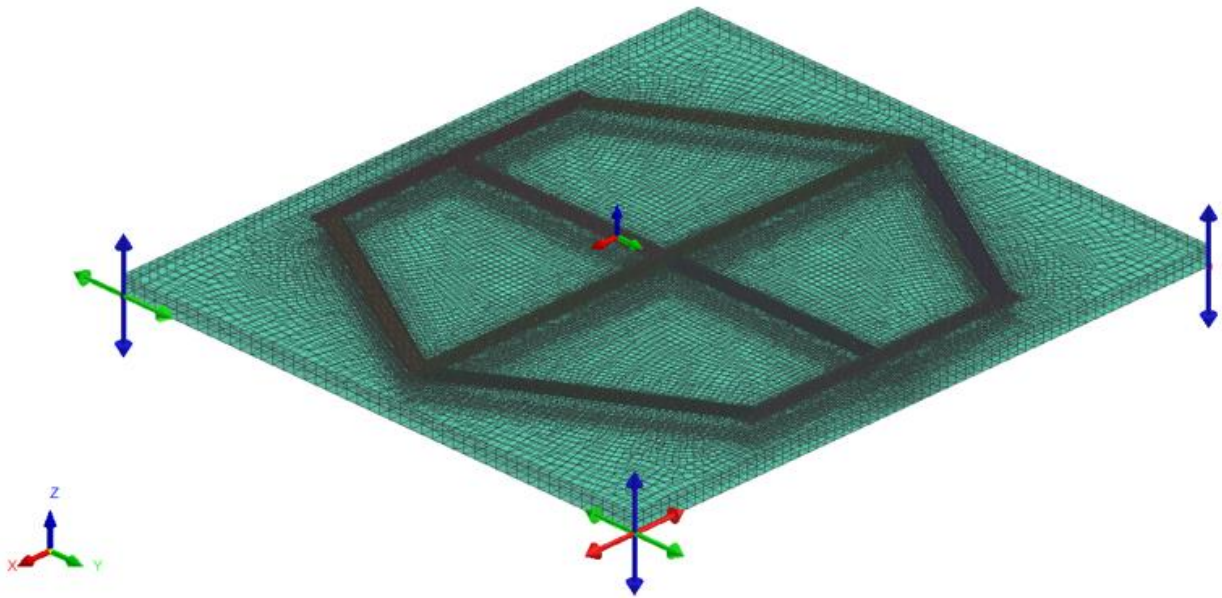


Figure 2. Mechanical boundary condition applied to avoid rigid body motion

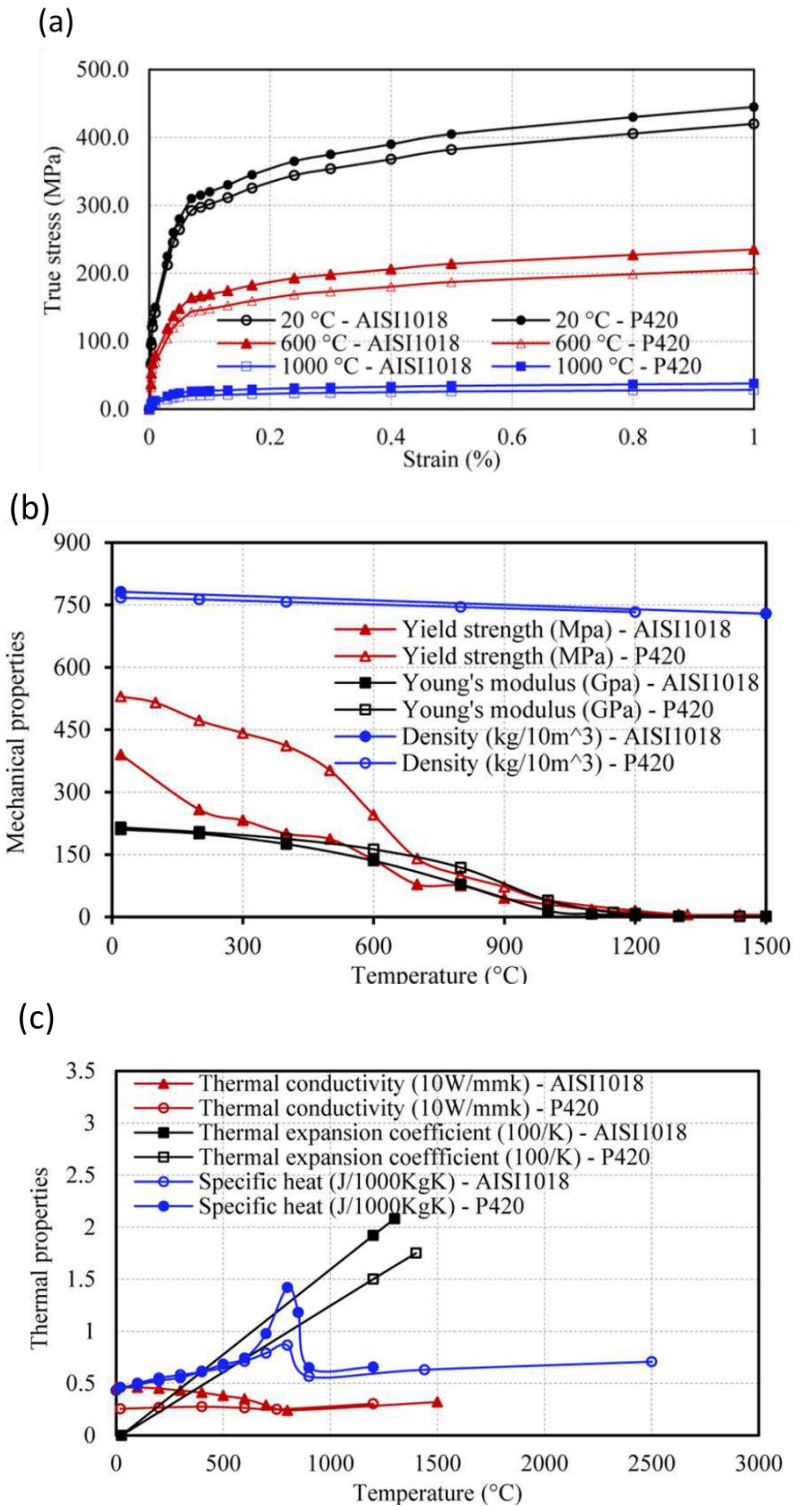


Figure 3. (a) Stress-strain curve P420 stainless steel and AISI 1018 steel, (b) and (c) temperature dependent material curve for P420 stainless steel and AISI 1018

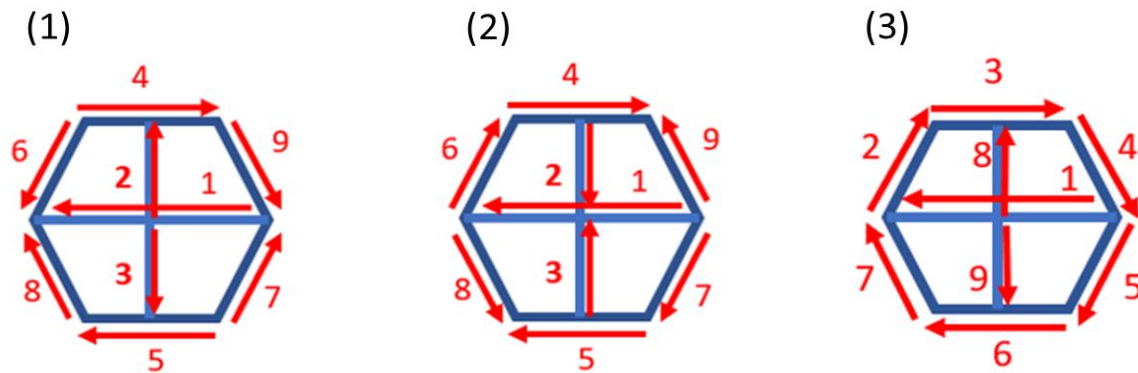


Figure 4. Path strategies three different deposition sequence and direction for one-layer hexagon

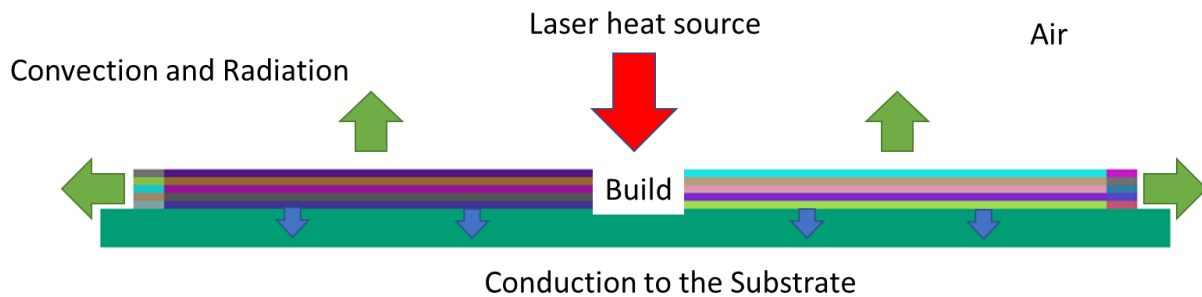


Figure 5. Thermal boundary condition on the build and substrate

2.2 Thermomechanical simulations

For the laser cladding DED process, the thermal history strongly influences the mechanical behavior. A 3D coupled thermal metallurgical mechanical FE model based on the commercial software SYSWELD was developed to investigate the thermo-mechanical behavior of the one layer and five layers hexagon. First, a 3D transient thermal analysis is used to calculate the temperature field. Secondly, the temperature results are used as the initial loading of a 3D quasi-static incremental analysis model to solve the stress problem [22]

2.2.1 Transient approach: moving heat source

When using the transient technique, calculations are made for each subsequent time step, which is automatically calculated depending on the mesh density of the model. In this type of analysis, the mathematical model of the heat source follows the path that determines the deposition trajectory. In this case, the parameters used to describe the heat source model are the laser cladding process parameters, such as the velocity, material feed rate and the thermal efficiency of the process. Currently, the conical model with a Gaussian distribution is most commonly used.

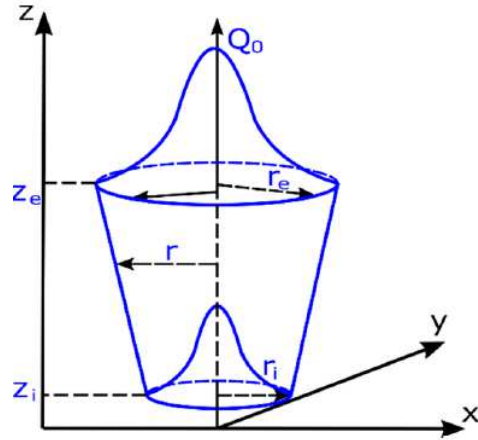


Figure 6. 3D conical Gaussian model of the heat source

$$Q(x, y, z) = Q_0 \exp\left(-\frac{x^2 + y^2}{r_0^2(z)}\right) \quad (1)$$

$$r_0(z) = r_e + \frac{r_i - r_e}{z_i - z_e}(z - z_e) \quad (2)$$

Where Q_0 is the maximum value of the volumetric heat flux density, r_e and r_i are upper and lower of cone diameter; z_e and z_i are cone length parameters; x, y, z are nodes coordinates.

Equation (1) is the volumetric heat flow density into material with respect to nodes coordinates. Equation (2) supplements Equation 3 by defining the radius change in the depth direction [23]. This method of defining the heat source model and performing numerical analyses needs calibration of the heat source. During this stage of the simulation, inaccurate calibration of the heat source model leads to errors and incorrect results. Figure 7 shows an example of the heat source model calibration procedure.

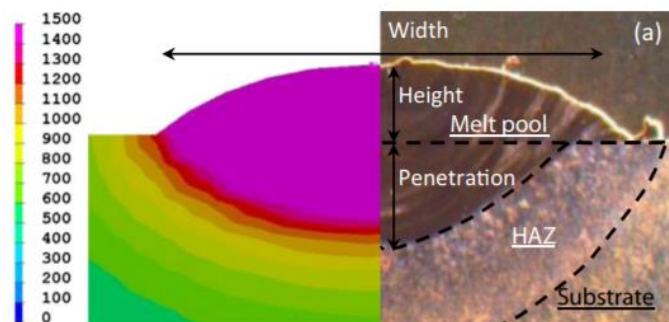


Figure 7. Example of calibration of heat source parameters by comparing the analysed shape and size of the melt pool and heat affected zone with a real macrograph of the laser bead.[24]

The analysis using the transient technique is divided into three parts: preparation of the material base, the thermal and related metallurgical changes, and the mechanical characteristics calculations such as the residual and Von Mises stresses and displacement distributions, etc. [23]. With the calculation being performed each time, the user is provided with a powerful set of thermo-metallurgical and mechanical data related to the simulated process after completing the

analysis. This complex solution comes at the cost of an extended calculation time. This is the primary reason that there are other calculation techniques used when calculating large and complex structures. However, such a large amount of data, including distribution of temperatures, hardness, the metallurgical phases, stresses, and deformations make it an ideal solution to analyse the local effects of laser cladding process.

For this research, the heat source parameters were set as following: energy per unit length, 110 J/mm; welding speed, 8 mm/s; arc heat efficiency, 0.9; length, width, depth of conical heat source model, 4, 3, 2 mm. The element birth and death technique along with moving heat source was used. In this technique, all the elements of the entire model are created at the beginning. All the deposited elements are initially deactivated and then gradually activated following the movement of the heat source.

2.2.2 Imposed thermal cycle

As already mentioned, the "transient" technique is practically impossible to use during calculations of numerical large and complex components as an analysis tool due to the amount of data generated and the computational cost. In these cases, the imposed thermal cycle technique is used [25][14]. In a way, this is an extension of the "transient" technique, which involves applying a proper thermal cycle to the group of elements within a bead section simultaneously.

Based on the resultant temperature profile, the average thermal cycle for the nodes on the molten zone is calculated. As a standard procedure, the thermal cycle is prepared based on a simple model "transient" analysis. The cycle is then applied successively to all elements of the bead. The difference between the transient approach with the moving heat source and the imposed thermal cycle approach is that in transient approach the number of time steps or calculation cards are equal to the number of elements in the grid on the trajectory line. However, in the imposed thermal cycle approach the number of time steps are equal to the number of nodes being used to describe the imposed thermal cycle for that area. That is why the computation time is much less in imposed thermal cycle technique comparing with transient technique.

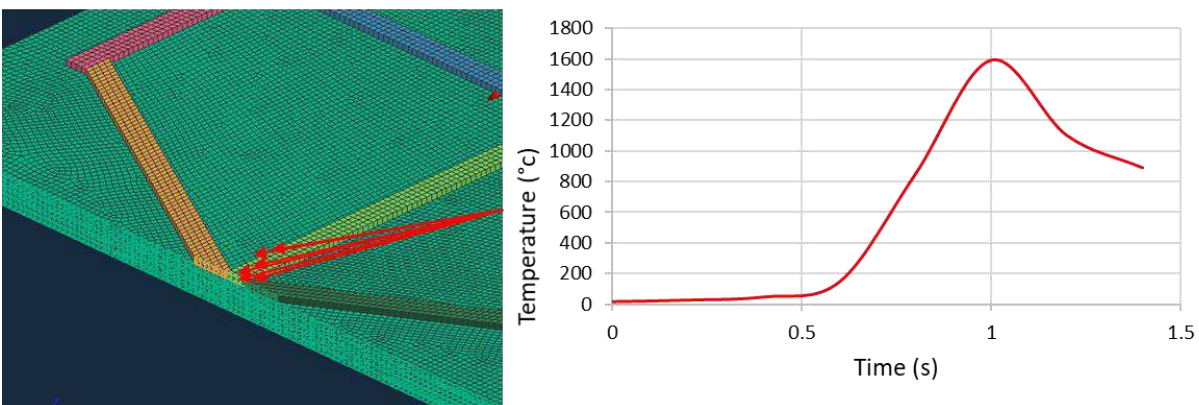


Figure 8. The imposed thermal cycle averaged from the thermal cycle of nodes in the molten pool

2.2.3 Thermal analysis

In the SYSWELD solver the calculation of the temperature fields is based on the Fourier differential formula. It is necessary to obtain the temperature dependence of the heat conductivity coefficient, specific heat capacity, and density [26].

$$\frac{\partial T}{\partial t} = \frac{\lambda}{c \cdot \rho} \left(\frac{\partial^2 T}{\partial x^2} + \frac{\partial^2 T}{\partial y^2} + \frac{\partial^2 T}{\partial z^2} \right) = \alpha \nabla^2 T \quad (3)$$

$T(K)$ is the temperature, $t(s)$ is time, x, y, z (m) are the nodes coordinates, α (m^2s^{-1}) is the thermal diffusivity coefficient, λ ($W.m^{-1}K^{-1}$) is the heat conductivity coefficient, c ($J.Kg^{-1}K^{-1}$) is the specific heat and ρ ($kg.m^{-3}$) is the mass density [26].

Heat convection equation with respect to coupled thermal metallurgical analysis is presented by the equation 4.

$$\left(\sum_i P_i (\rho C)_i \right) \frac{\partial T}{\partial t} - \nabla \cdot \left(\left(\sum_i P_i \lambda_i \right) \nabla T \right) + \sum_{i < j} L_{ij}(T) \cdot A_{ij} = Q \quad (4)$$

P is the the phase proportion, ij phase index, Q is the heat source, $L_{ij}(T)$ is the latent heat of $i \rightarrow j$, A_{ij} proportion of phase i transformed to j in time unit [26].

2.2.4 Mechanical analysis

The mechanical model is the second step of the current analysis. The previous thermal histories are utilized in this step of the analysis as the thermal loading for the stress evolution at the end of the analysis which is left in the build part as residual stress. In the mechanical analysis, the same finite element mesh was employed as in the thermal analysis. According to Hooke's law, the stress tensor is related to elastic strain [27]:

$$\sigma = D \cdot \varepsilon^e \quad (5)$$

where D is the elastic stiffness matrix determined by Young's modulus (E) and Poisson's ratio (ν). The total strain increment can be composed of the following components [27][28]:

$$\Delta \varepsilon = \Delta \varepsilon^e + \Delta \varepsilon^p + \Delta \varepsilon^t + \Delta \varepsilon^v \quad (6)$$

where ε^e , ε^p , ε^t are elastic, plastic, and thermal strain, respectively. ε^v is the volumetric strain induced by the phase transformation. The thermal strain $\Delta \varepsilon^t$ is calculated as [27]:

$$\Delta \varepsilon^t = A \Delta T \quad (7)$$

$$AT = \beta [1 \ 1 \ 1 \ 0 \ 0 \ 0] \quad (8)$$

$$\Delta \varepsilon^t = A \Delta T \quad (9)$$

$$AT = \beta [1 \ 1 \ 1 \ 0 \ 0 \ 0] \quad (10)$$

where ΔT is the temperature increment, β shows the temperature dependent coefficient of thermal expansion.

The elastic strain increment component $\Delta \varepsilon_{ij}^e$ can be described by the stress component σ_{ij} [27].

$$\Delta \varepsilon_{ij}^e = \frac{1 + \nu}{E} \Delta \sigma_{ij} - \frac{\nu}{E} \Delta \sigma_{kk} \delta_{ij} \quad (11)$$

where δ_{ij} is Kronecker delta. Plastic strain is caused by yield and strain hardening, σ_{ij} is deviating stress and σ_{kk} is the hydrostatic pressure. In this model, isotropic hardening is assumed at the plastic zone, and the plastic strain increment according to the normality rule can be calculated as [27]:

$$\Delta \varepsilon p = \frac{1}{3} \Delta \varepsilon p I + \Delta \varepsilon q n \quad (12)$$

Where n is the flow direction, and I is a unit matrix. p and q are the two directions that are perpendicular to each other. εp and εq can be calculated by the equation Eqs. [18], [20], [21]:

$$\phi(p, q, H\alpha) = 0 \quad (13)$$

$$\Delta \varepsilon p \frac{\partial \phi}{\partial q} + \Delta \varepsilon q \frac{\partial \phi}{\partial p} = 0 \quad (14)$$

In the above equations, $H\alpha$ is a set of hardening parameters, and p, q and $H\alpha$ are defined by the following Eqs. [27], [31], [32]:

$$p = p^{el} + K \Delta \varepsilon p \quad (15)$$

$$q = q^{el} + 3G \Delta \varepsilon q \quad (16)$$

$$\Delta H\alpha = h^\alpha(\Delta \varepsilon p, \Delta \varepsilon q, p, q, H\beta) \quad (17)$$

where $H\beta$ is the hardening modulus with G and K being the shear and bulk modulus.

2.3 Geometric analysis methodology comparing simulation results

To quantitatively compare the residual and Von Mises stress results, a structured methodology for directly comparing the observed residual stress patterns developed by Urbanic et al. [33] is utilized. This is extended where images from the results models are converted into topology and 'raster' data via image analysis and geometry creation tools using Rhino® CAD tools and the Grasshopper® visual programming language and VBA. Each stress colour coded range in the legend is classified into a z height. A point cloud data set is generated for the desired level of granularity to provide positional residual stress data in a geometric format, as shown in Figure 9. From this point set, quantitative comparisons are performed using Excel.

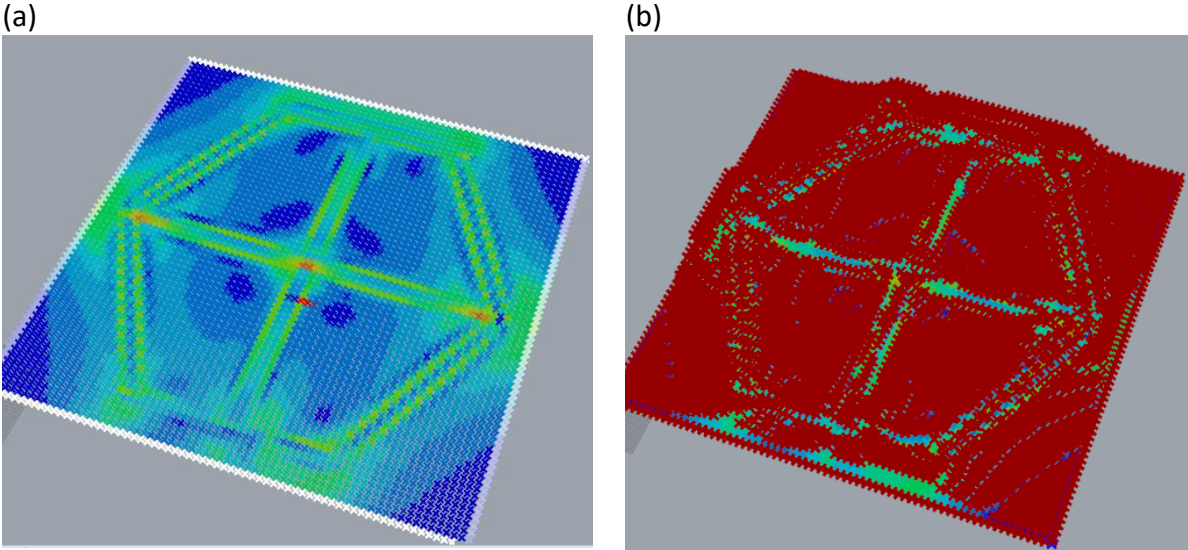


Figure 9. (a) The Von Mises stresses for the Hex1 configuration with x,y points, and (b) the topology point set, where the z height for each (x, y) point is associated with a stress level.

3 Results and discussion

3.1 Stress results

Comparisons of the build scenario for the Von Mises stress distributions for the 3 different deposition path strategies for the one-layer hexagon after the parts are cooled to room temperature, via transforming the images into point cloud data results are illustrated in Figure 10. A 70 x 70 point grid is created (4900 points) for the analyses. The Excel conditional formatting is applied to create the color maps. The gradient scale varies from green to yellow to red based on the data values. Therefore, graphs with filtered data (Figure 10) or the graphs where a difference map are presented also illustrate the fill color range (Figure 10).

It is quite apparent that the Hex 3 configuration has the greatest amount of zero to very low stress islands. There are several large islands in the interior regions for Hex 3 and these zero to very low stress islands comprise 13% of the results. For the Hex 1 and Hex 2, the zero to low stress region comprise 9 and 10% of the results respectively. Conversely, the moderately low stress regions for the Hex 2 are approximately 4% greater than the Hex 3 and Hex 1 configurations, which are almost equivalent (~29%). Extracting the medium to high stress regions clearly highlights that the top edges and the centre cross have higher stress regions for the Hex 1 and Hex 2 configurations, whereas these are medium stress regions for the Hex 3 configuration. The acute angle 3 point junctions (furthest left and right junctions) have the highest stress regions for all configurations. Interestingly, the high stress patterns are very similar for all configurations for both the left and right joints, which may be due to overlap conditions. This pattern is illustrated in Figure 11. The data is restructured to mirror the results to illustrate the similarities.

Von Mises Stress Map

Low – Mid Stress Map

Mid – High Stress Map

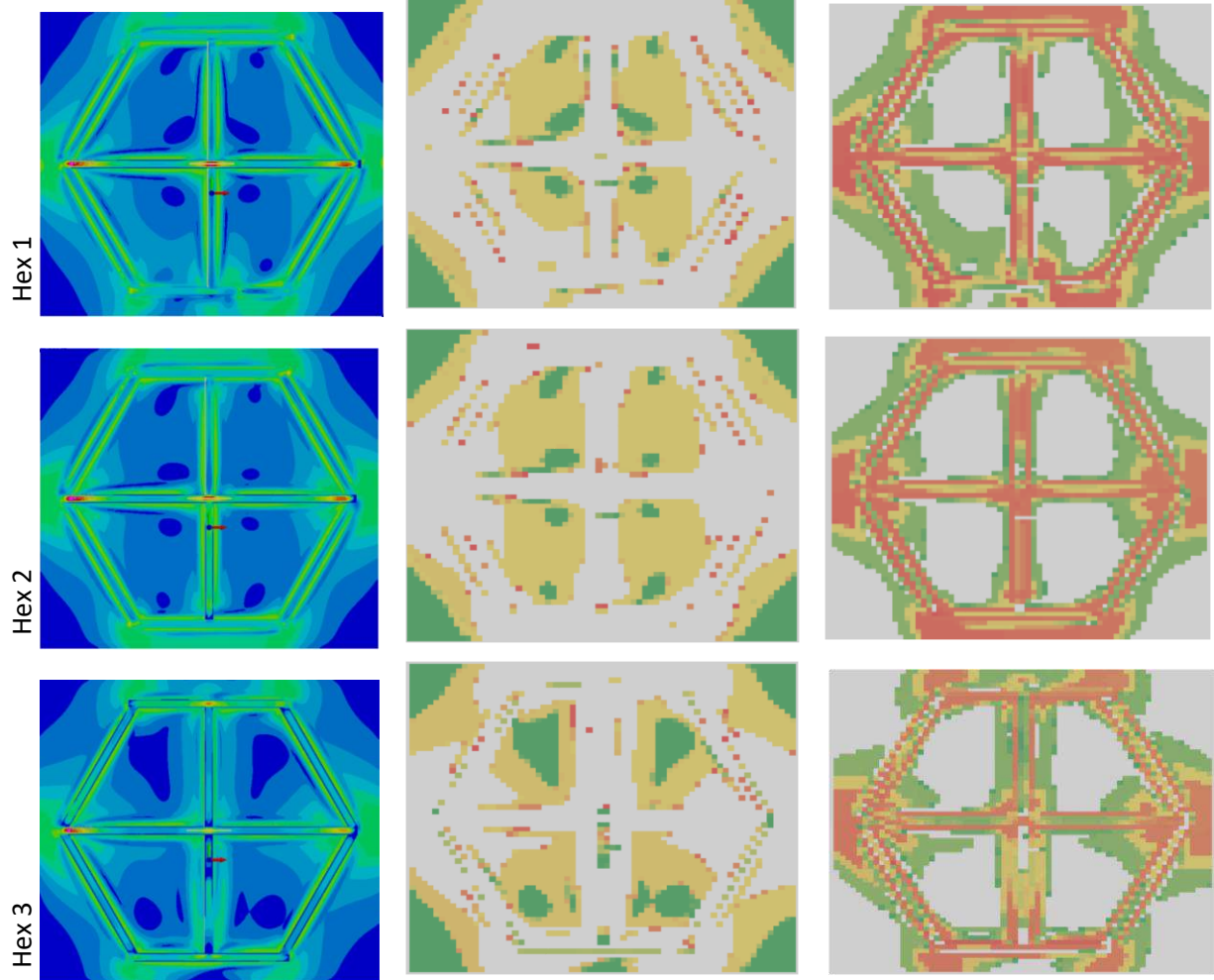
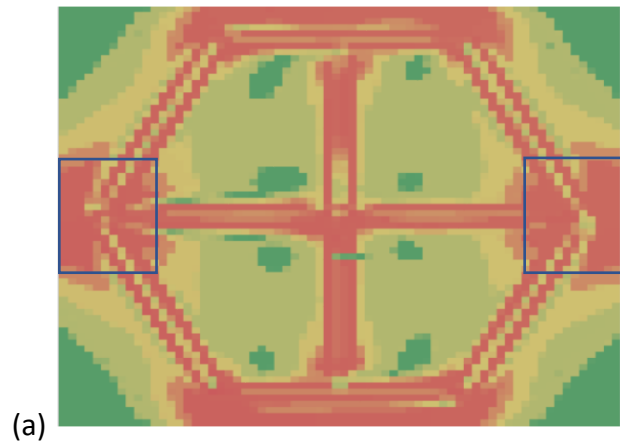


Figure 10. The Von Mises stress images, and filtered stress regions for the three different deposition path strategy



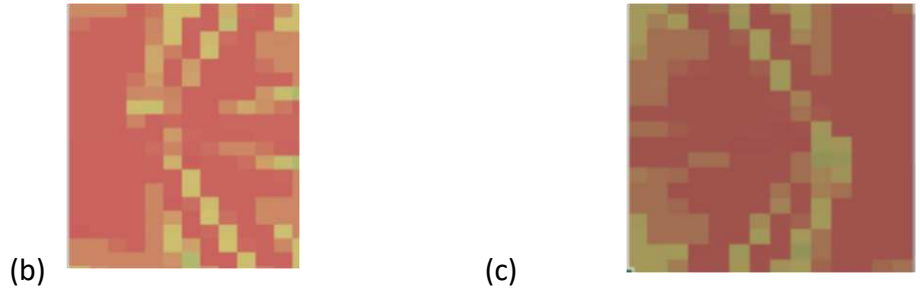


Figure 11. (a) The Hex 2 Von Mises stress map in Excel, (b) the enclosed left joint data for Hex 2, and (c) the enclosed right joint data for Hex 2.

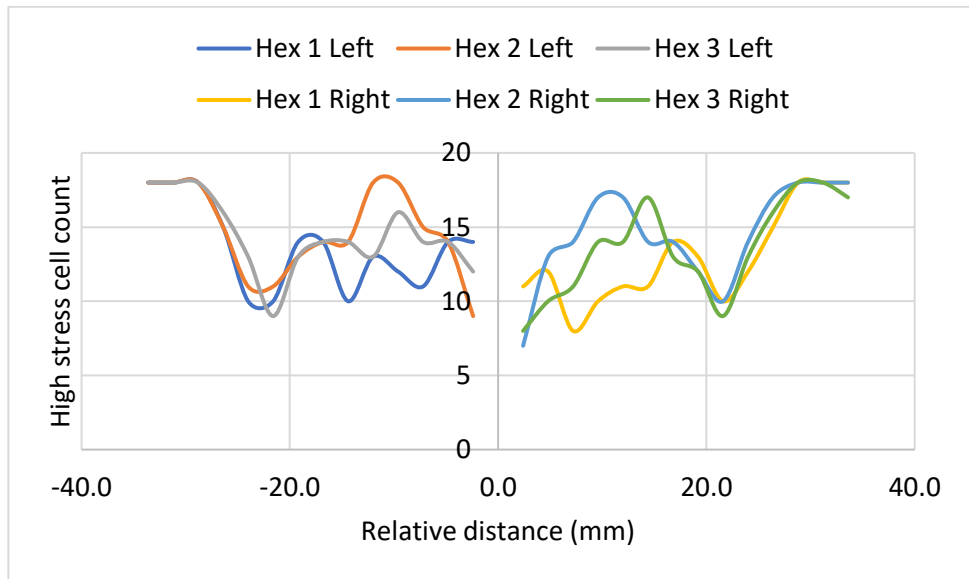


Figure 12. Enumerating the number of high stress cells for the left and right joints, and comparing the three build strategies.

A comparison between Hex 2 to Hex 1, and Hex 3 to Hex 1 is done to quantitatively determine the configuration that has the minimum stress configurations. For the Hex 2 to Hex 1 set, it can be seen that most of the regions (62%) have a light orange/yellow colour, which indicates that there is no difference between the Von Mises stress results for the two case studies being compared. This includes much of the bead deposition regions as well as the substrate. The orange red tones indicate a negative difference in stress values, and the green values indicate a positive difference in stress values. Interestingly, the quantification results indicate that both regions are 19%. When determining the solution with the overall lowest stresses, the discontinuous build solution provides similar results when considering the results as a whole. This is not true for the Hex 3 to Hex 1 case study. The zero difference region is 43%. However, there is a slightly greater proportion of negative difference stress values (30%), than the positive difference stress values (27%). This indicates that overall, the Hex 3 configuration has the overall lowest Von Mises stress solution. A radar graph (Figure 12) illustrates the stress difference patterns for each quadrant for the Hex 3 to Hex 1 comparison.

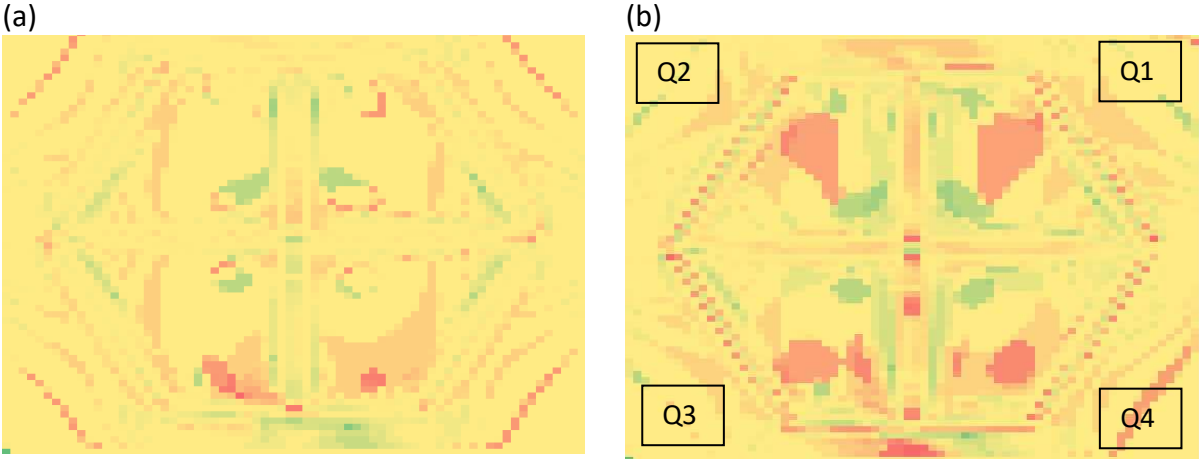


Figure 13. (a) The difference in Von Mises stresses for the Hex 1 and Hex 2 configurations and (b) difference in Von Mises stresses for the Hex1 and Hex 3 configurations, where red indicates a large negative stress difference, and green indicates a large positive stress difference.

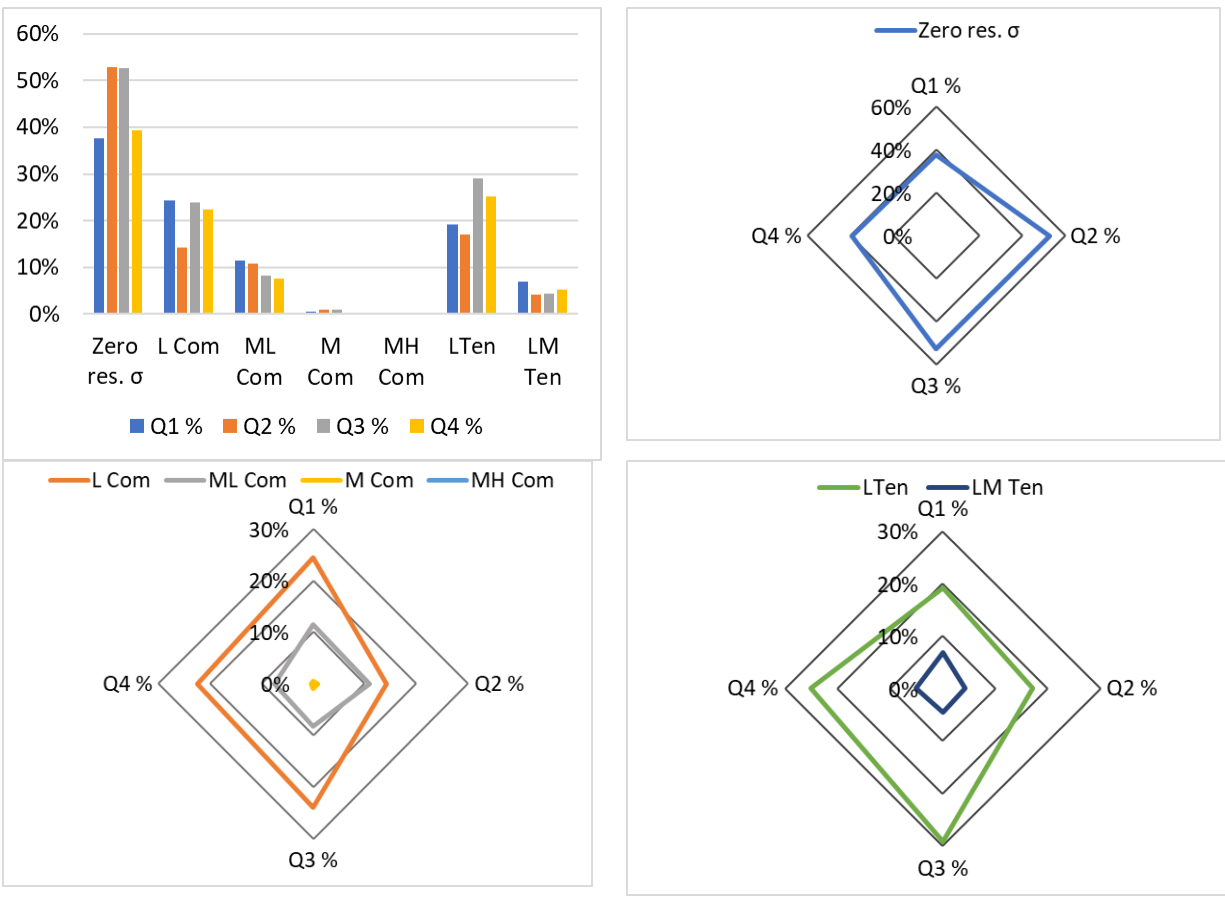


Figure 14. (a) The difference in Von Mises stresses for the Hex1 and Hex 3 for each quadrant (b) difference in Von Mises stresses for the Hex1 and Hex 3 configurations, where red indicates a large negative .

The Von Mises stress has been measured and compared at the concerned areas along the lines AB, BC and CD on top of the bead as shown in Figure 15. The Von Mises stress along the lines AB, CD and EF on top of the bead is lower for the Hex 3 version as shown in Figure 16. The longitudinal residual stress, xx on the similar lines has lower values for Hex 3 as depicted in Figure 17.

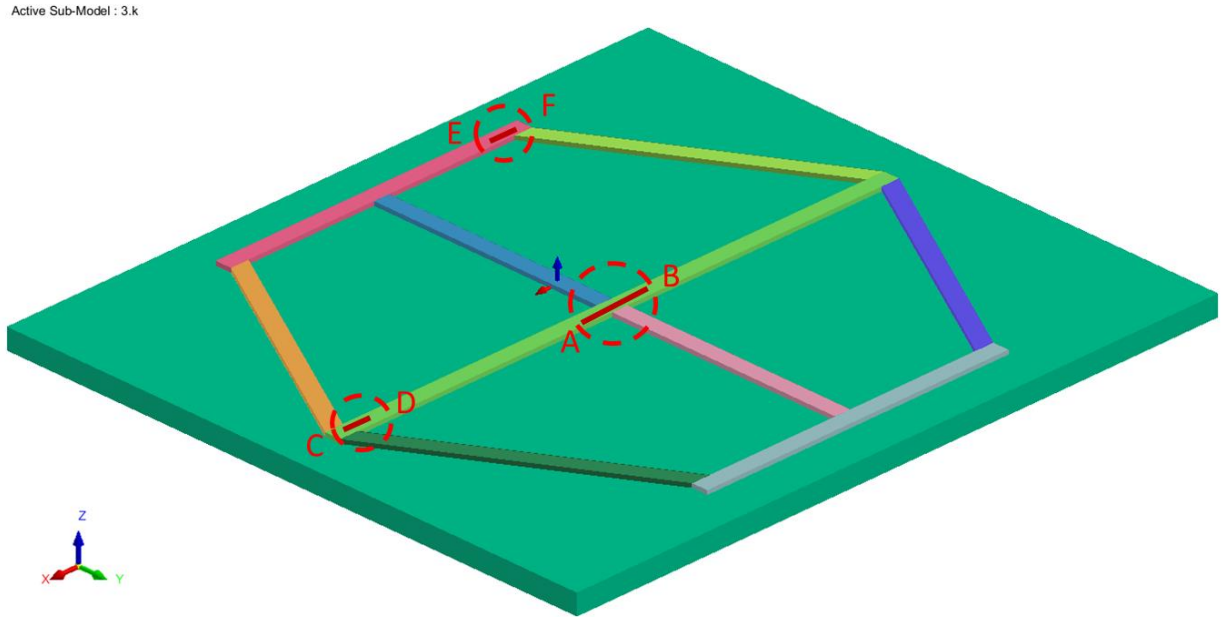
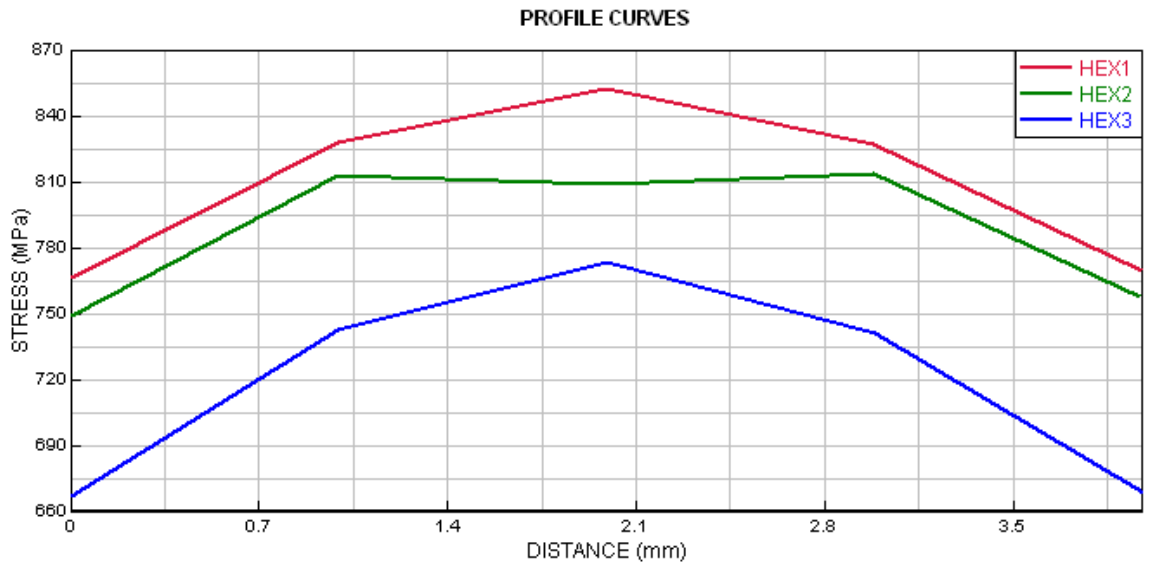


Figure 15. The considered paths for the Von Mises stress and the XX residual stress comparison in three different path strategies



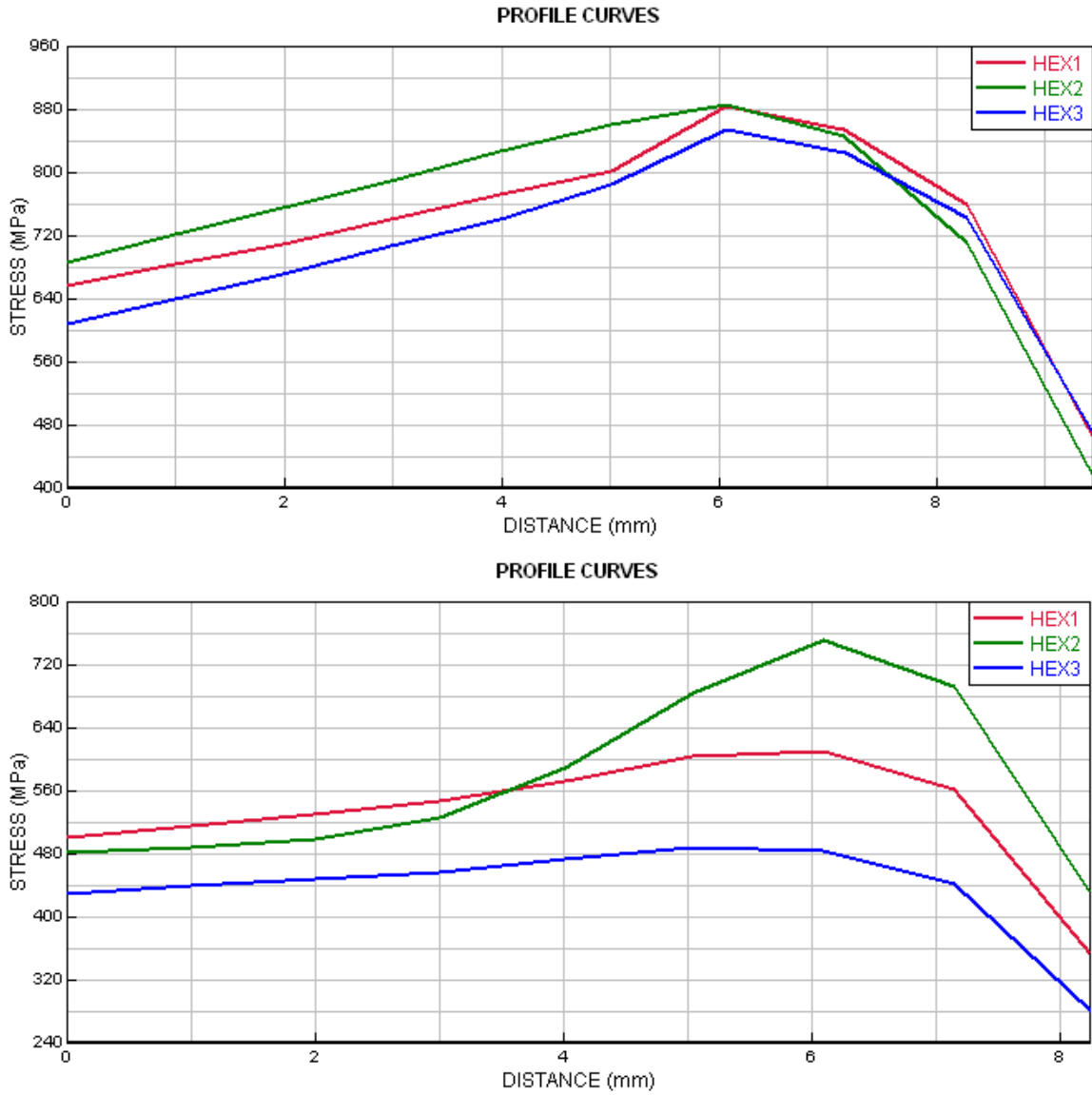
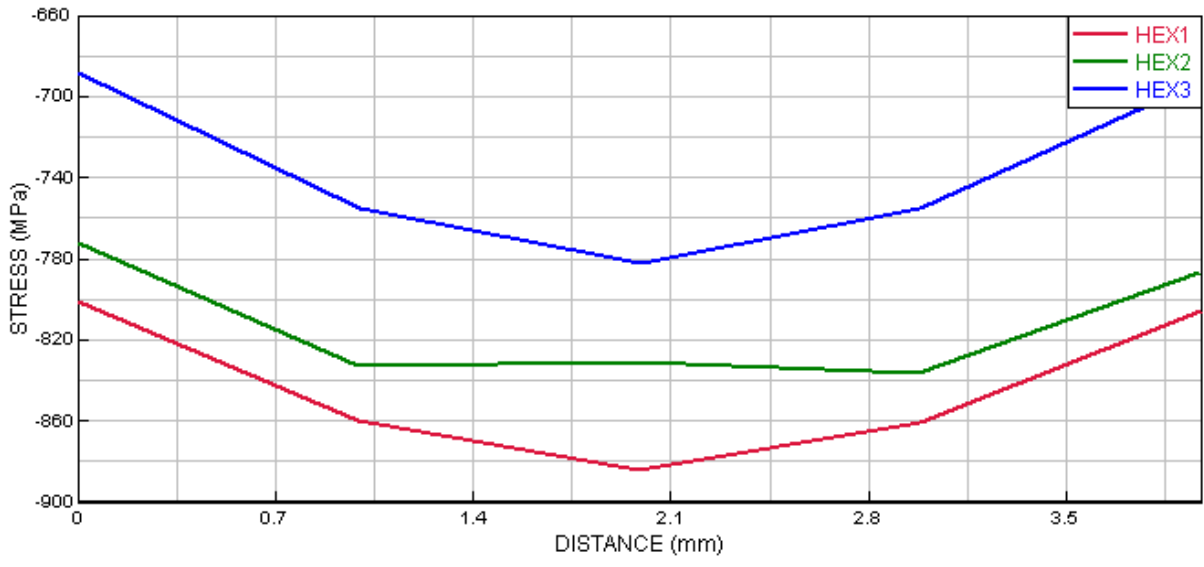


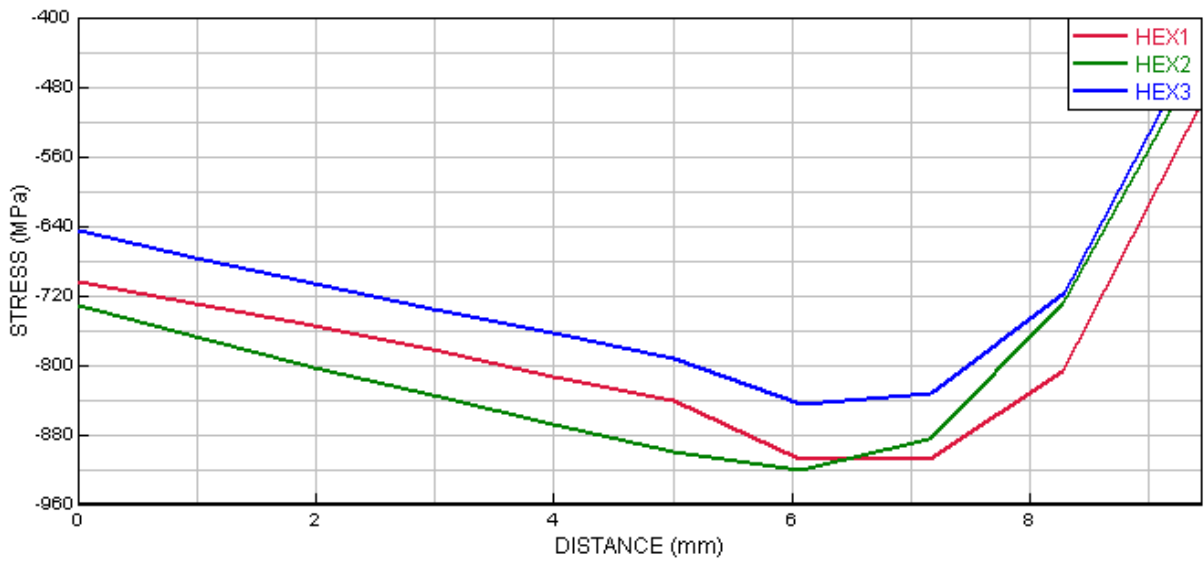
Figure 16. The Von Mises stress comparison along lines (a) AB, (b) CD and (c) EF

The xx residual stress comparison along the lines AB, CD and EF for deposition paths.

PROFILE CURVES



PROFILE CURVES



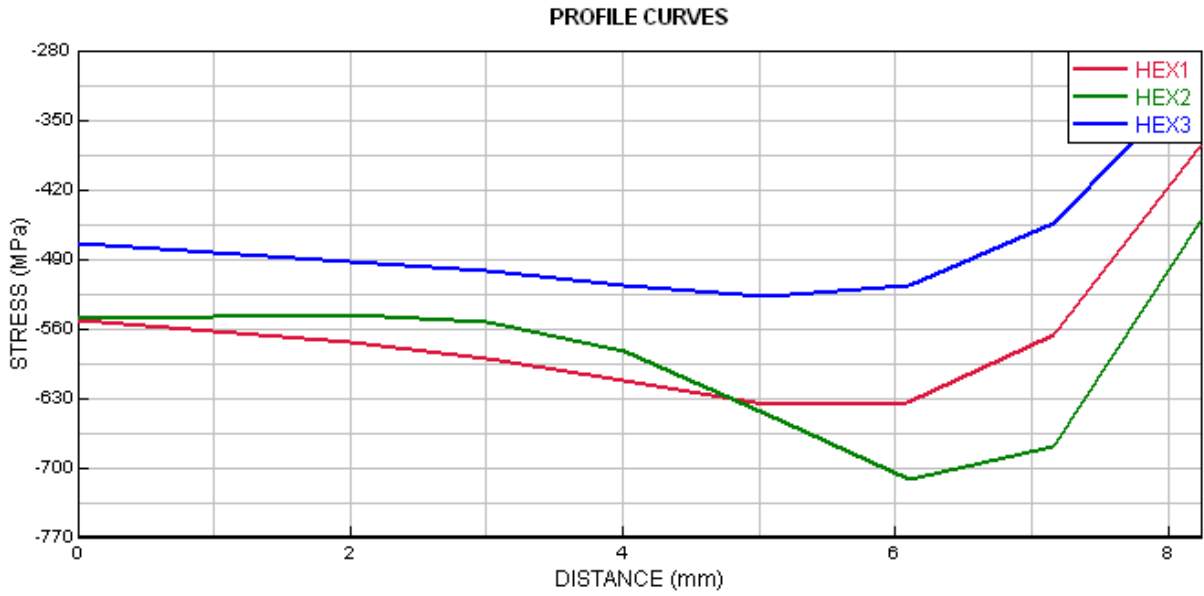


Figure 17. The xx stress comparison along lines (a) AB, (b) CD and (c) EF

The YY residual stress along the line GH as shown in Figure 18. The yy compressive stress was slightly lower for the Hex 3 as compared to the other two versions, as shown in Figure 19

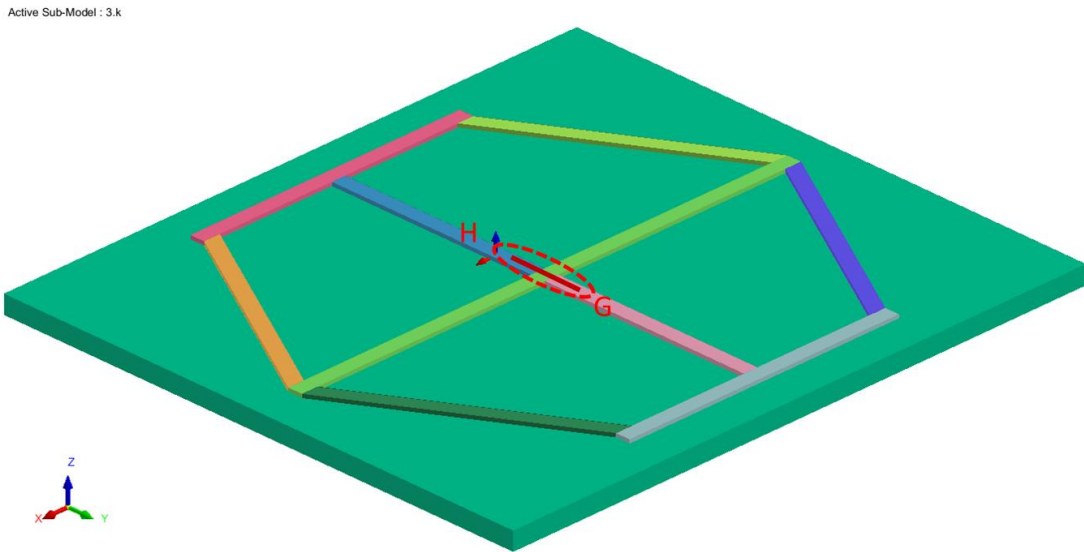


Figure 18. The considered paths for the YY residual stress comparison in three different path strategies

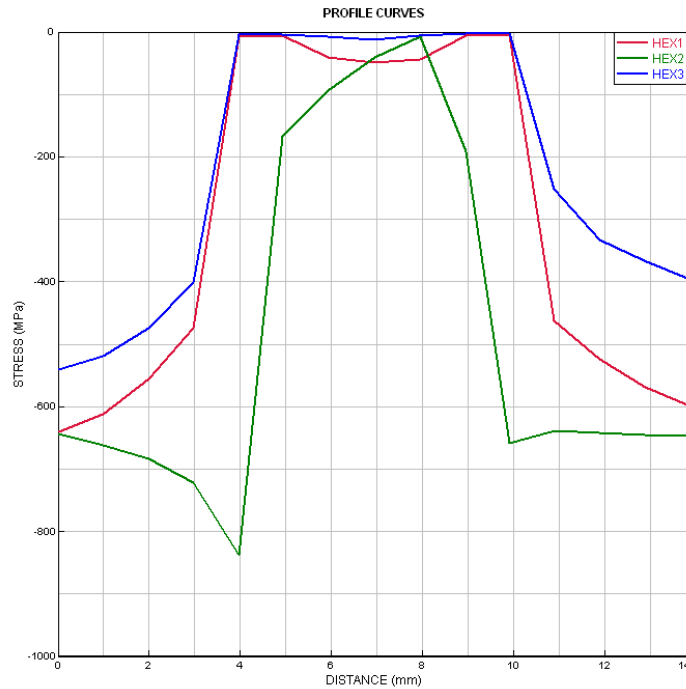


Figure 19 . The YY stress comparison along line GH

Similarly, the residual stress in the normal direction, ZZ, was measured and plotted along the line IJ, Figure 20. It can be seen that the Hex 3 has values closer to zero, Figure 21.

Active Sub-Model : 3.k

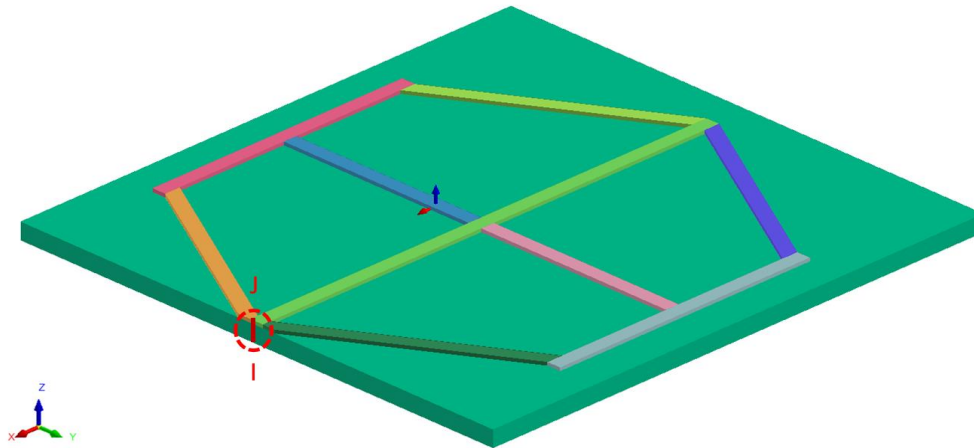


Figure 20. The considered paths for the ZZ residual stress comparison in three different path strategies

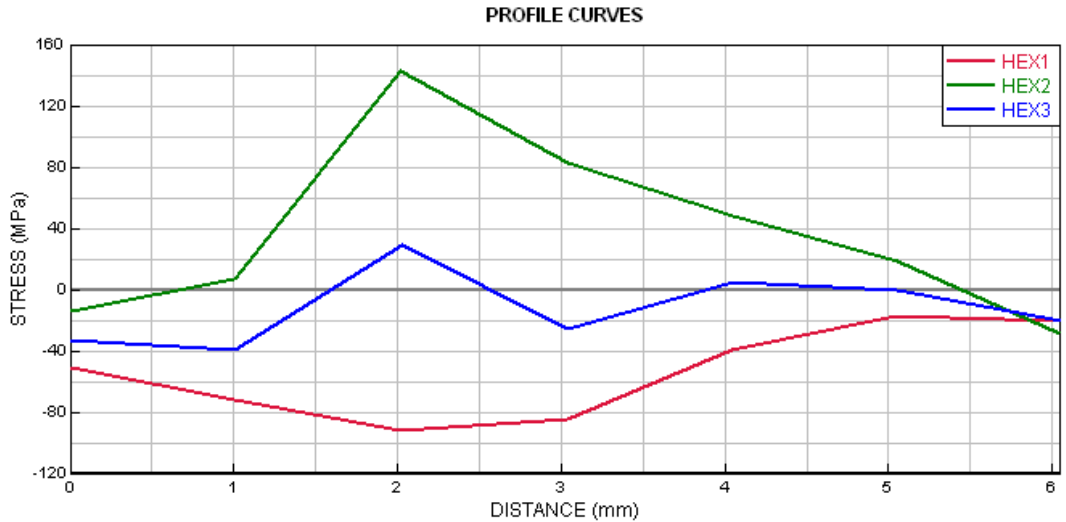


Figure 21. The zz stress comparison along line IJ

The comparison of stresses on selected areas showed that the Hex 3 deposition path has better performance in terms of lower amounts of residual stress. Consequently, the Hex 3 path deposition sequence is selected to investigate the imposed thermal cycle approach and enhancing to the multilayer model.

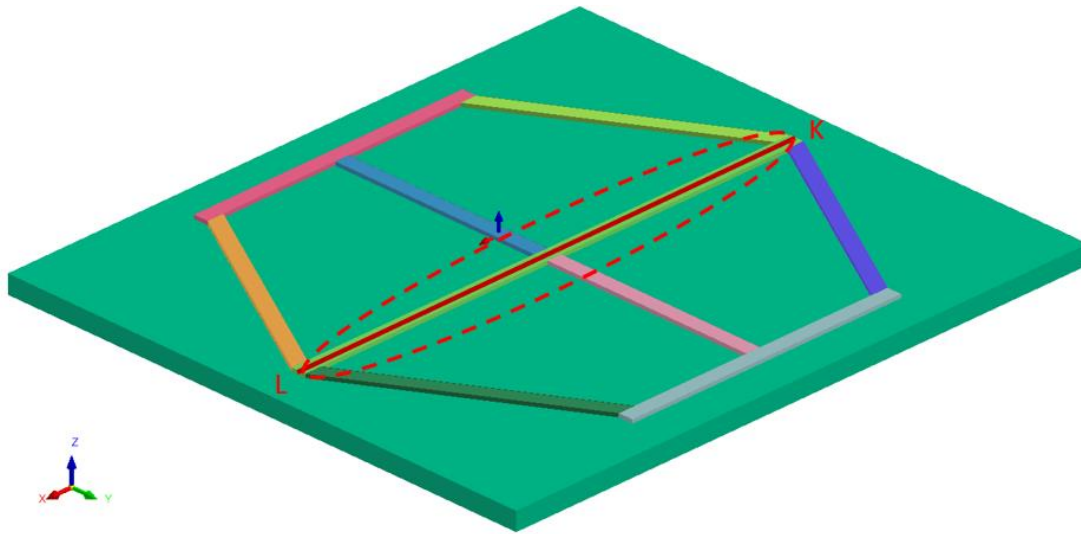
Both the longitudinal and transversal residual stresses are compression stresses for the selected lines for all three deposition strategies. Thermal expansion leads to plastic deformation during the deposition process, which puts the beads under compressive stress. A large tensile longitudinal stress is generated in the deposition region due to shrinkage, while a compressive longitudinal stress is generated far away from the deposition wall.

Figures 17, 19 and 21 shows the comparison residual stress contour in XX, YY and ZZ direction.

The normal residual stress formation is weakly affected by deposition path sequence and direction however the longitudinal and transvers stress are significantly affected by path planning strategies with respect to sequence and direction.

3.2 A comparison of the macro bead technique and the transient technique

The imposed thermal cycle approach that uses the average temperature curves of the nodes in the melt pool was utilized and the results are compared with transient method for hex 3. The computational time employing the transient technique is five times of the macro bead technique for the one-layer hexagon. The comparison of Von Mises stress on the line KL is shown in Figure 22.



PROFILE CURVES

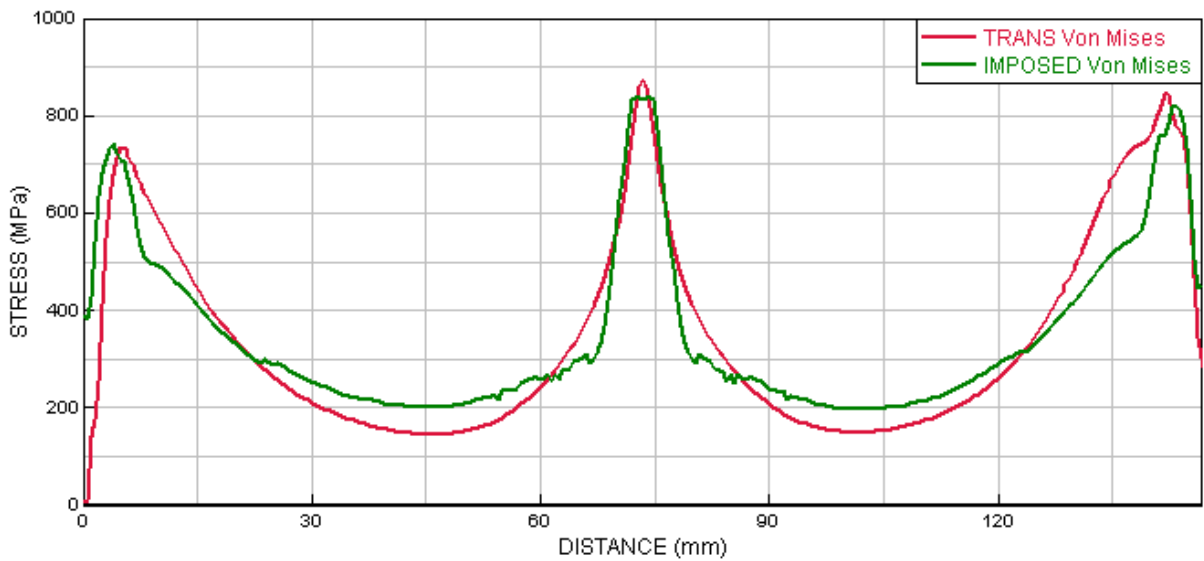


Figure 22. Von Mises stress comparison along the line KL for Hex 3 path using transient approach and imposed thermal cycle approach

The XX residual stress was compared along the line MN on the top of the bead after cooling the specimen. The compressive xx residual stress along the line MN for both techniques has a sharp decrease at the start, middle and end of the bead Figure 23. The reason for the sharp decrease at the start and the end of the bead in the transient approach is the laser igniting at the start and extinguishing at the end of the bead; and in the middle, is because of the re heating effects due to deposition of the vertical middle beads. For the imposed thermal cycle approach the thermal cycle is applied simultaneously to all the elements of the bead. Consequently, the effect of laser ignition and extinguishing is omitted and the effect of the reheat at junction areas is involved. As a result, the transition is smoother compared to the transient approach.

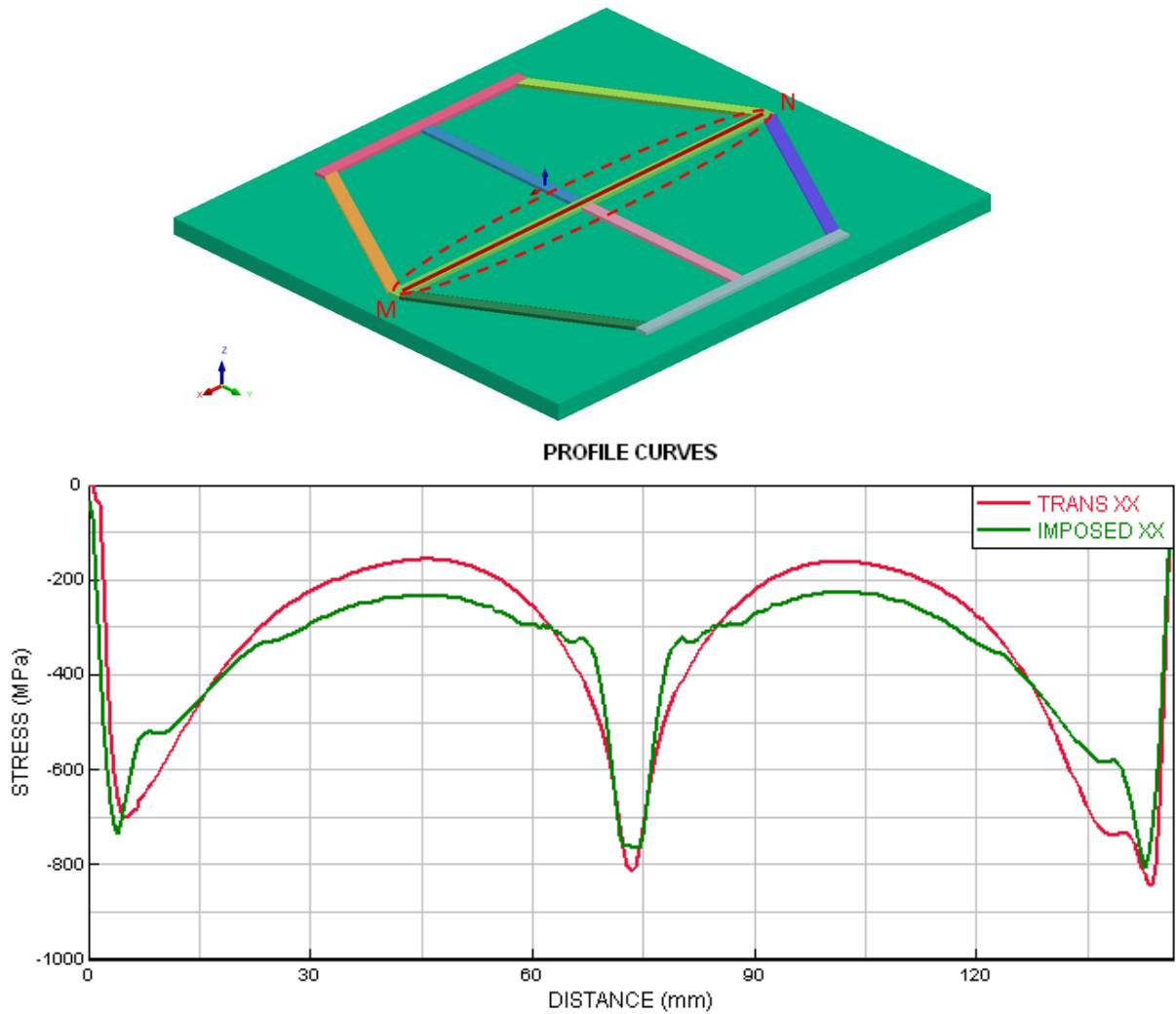
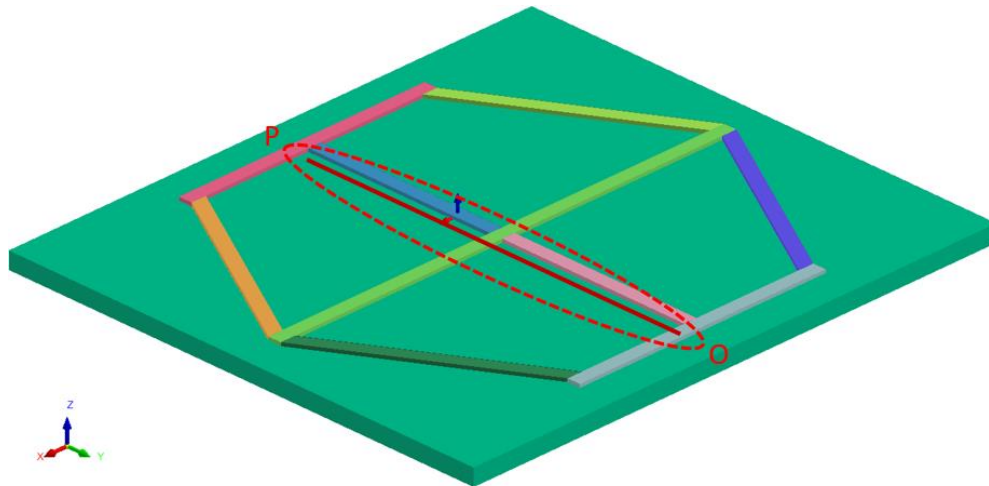


Figure 23. The XX residual stress comparison along the line MN for Hex 3 path using transient approach and imposed thermal cycle approach

The YY residual stress in transient and imposed thermal cycle approach are compared along the line OP on the substrate. In the middle zone on the substrate the maximum tensile residual stress is observed in both transient and imposed model, Figure 24. The laser ignition during deposition of middle bead in the middle zone may cause more residual stress comparing to the areas that laser extinguishes, closer the end of the OP line in transient model. In the imposed thermal cycle model, there is a similar pattern at the start middle and the ends due to the residual stress formation because of reheat when the other beads at the joints are deposited.



PROFILE CURVES

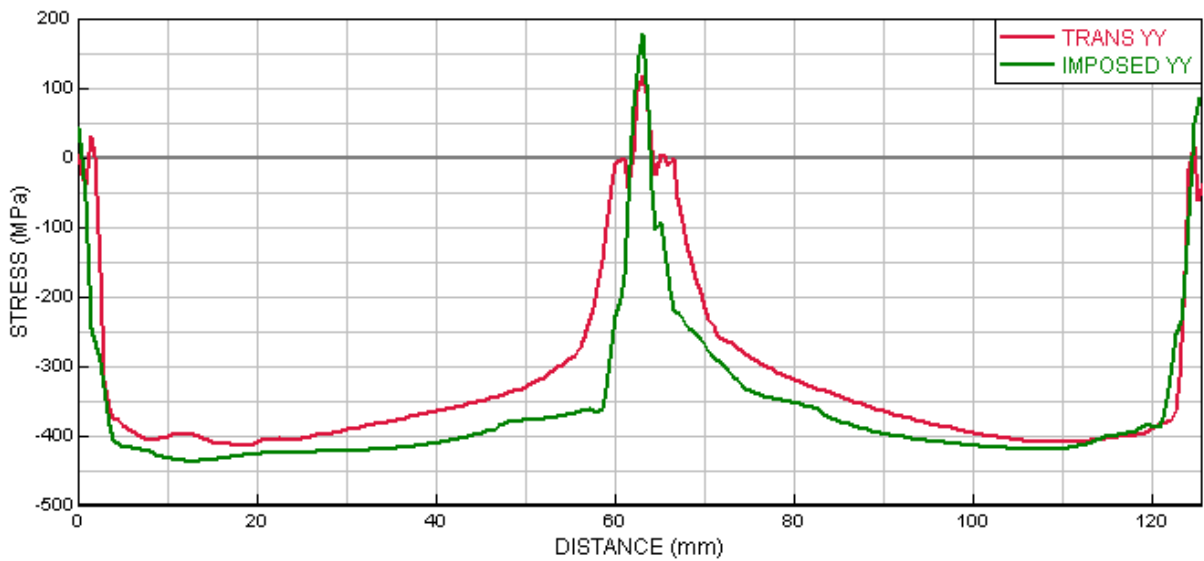


Figure 24. The YY residual stress comparison along the line OP for Hex 3 path using transient approach and imposed thermal cycle approach

The zz residual stress is being compared along the line QR starting from the top of bead to the substrate the normal stress in transient approach changes between 360 MPa to 0 and in the imposed approach varies between 210 MPa to 35 MPa (Figure 25).

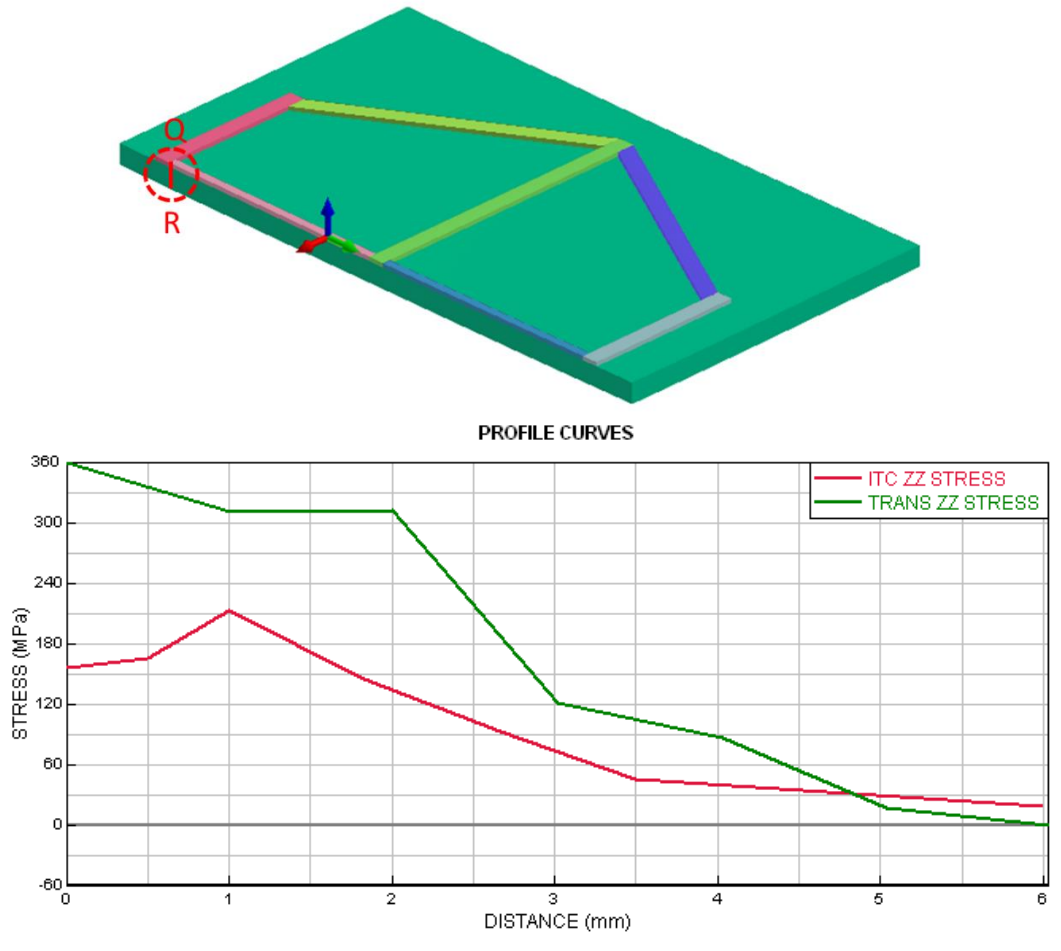


Figure 25. The ZZ residual stress comparison along the line QR for Hex 3 path using transient approach and imposed thermal cycle approach

3.3 5-layers study

There were two scenarios considered for the multi-layer deposition. The first one was a 5 layers deposition of martensitic stainless steel on a low alloyed carbon steel substrate using the macro bead technique and the second scenario was preheating the first three layers and deposition of two top layers implementing similar technique and considering the hypothesis of obtaining similar results to the first scenario in much less computational time. The first three layers were preheated to 100 °C for 20 second and deposition of fourth and fifth layer starts immediately after the preheat cycle was finished.

The comparison of stress results for both scenarios showed that the second scenario, preheated first three layers and two top layers deposited, can not be replaced by five layers deposition scenario since there is a sharp transient of stresses between the last preheated layer and the first deposited layer. Figure 26 shows the Von Mises stress changes along the line ST between the 3rd and 4th layers for both scenarios. As it can be seen there is 650 MPa difference between the maximum values on the considered path.

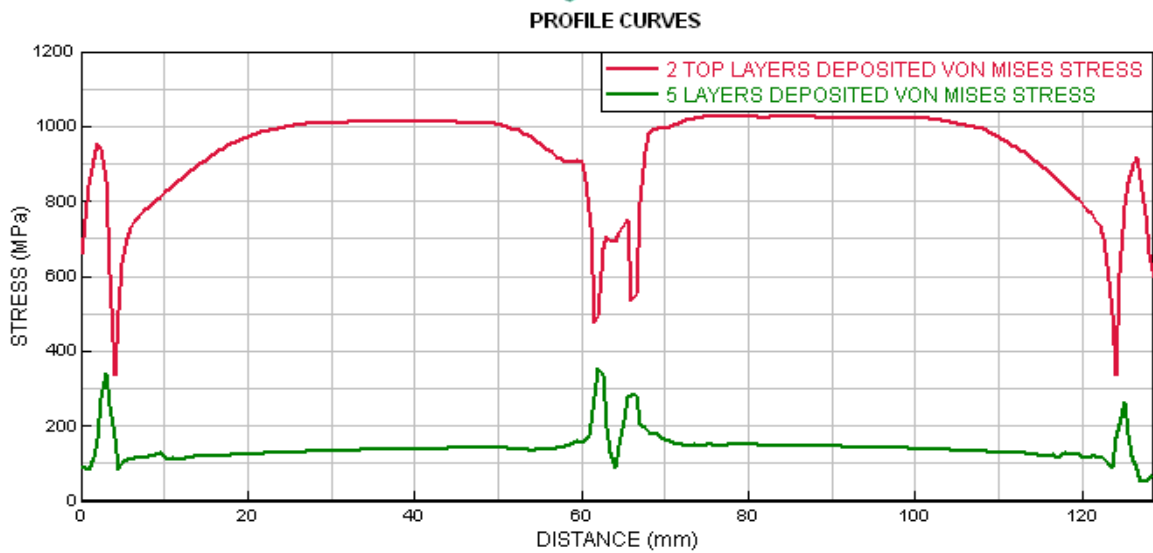
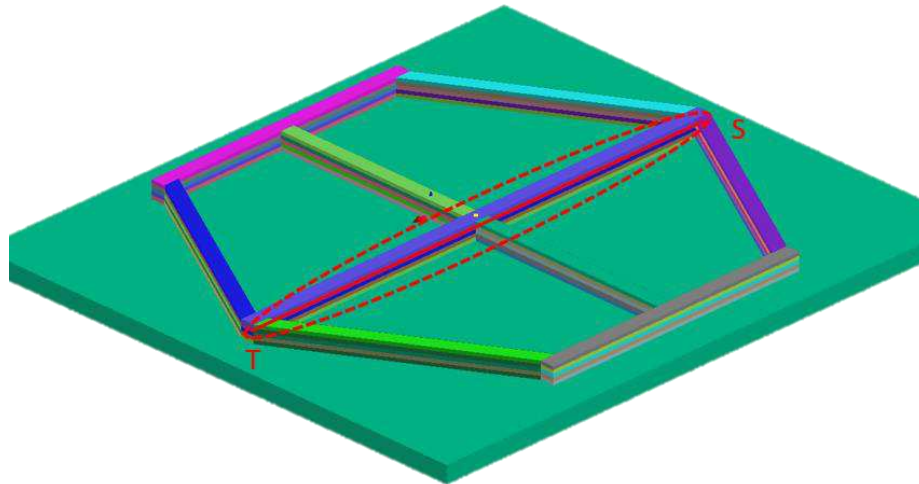


Figure 26. The Von Mises stress comparison along the line ST for 5 layers deposition and 3+2 layers deposition study

Thermal results

In order to study the thermal behavior of the different layers, the thermal cycle of the middle nodes on the top of first, second, third, fourth and fifth layers are considered. Figure 27 shows the nodes being considered and the thermal cycles of each node for the five layer deposition scenario. As shown in Figure 28, the peak temperature of the midpoint in the 1st layer decreases during deposition. As the thermal cycle is applied, the 1st peak of the thermal cycle occurs for this node. The dashed line is the melting temperature of P420 stainless steel. The second and third peak occurs when middle beads are being deposited and the middle point is thermally affected. The fourth peak occurs when the thermal cycle is applied to the top bead in the second layer. During the deposition of the second layer, the molten pool formed in the middle point of the 2nd layer, remelts the middle point of first layer. As it is above the melting point, there is a remelting effect. The midpoint of the 1st layer rises in temperature when the 3rd, 4th and 5th layer is deposited but does not remelt.

The peak temperature reduction of the first layer middle point, from the 2nd layer to the 5th layer is due to heat dissipation and gradual distance from the imposed thermal cycles in top layers. As a result, this point has experienced multiple post heating effects.

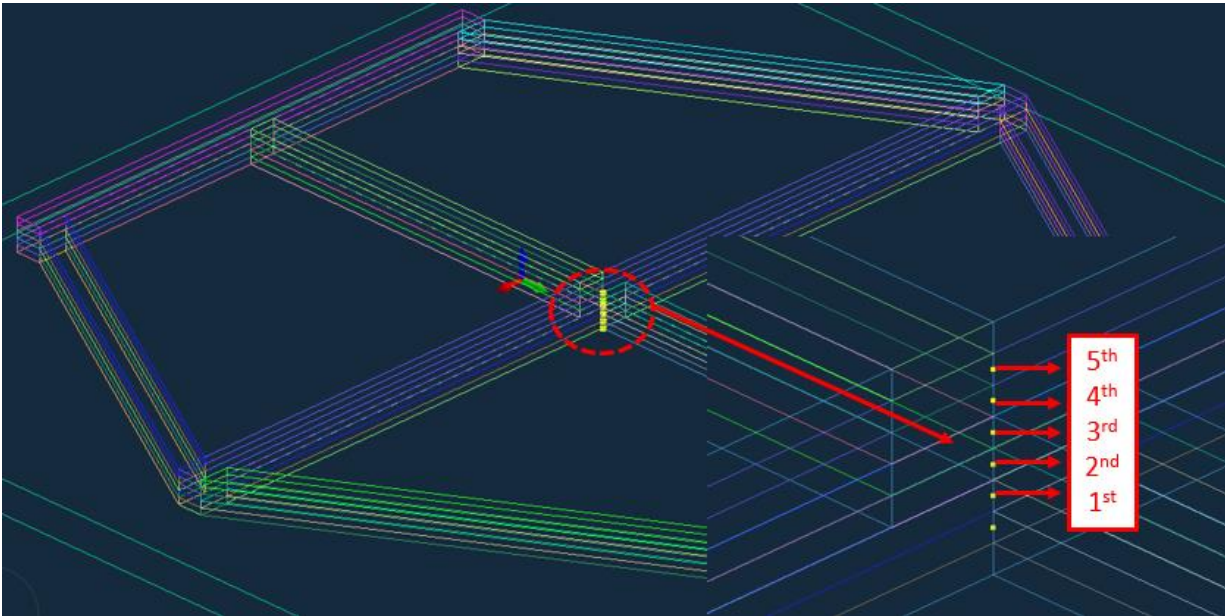


Figure 27. The nodes in the middle zone on top of each layer considered for thermal effects study.

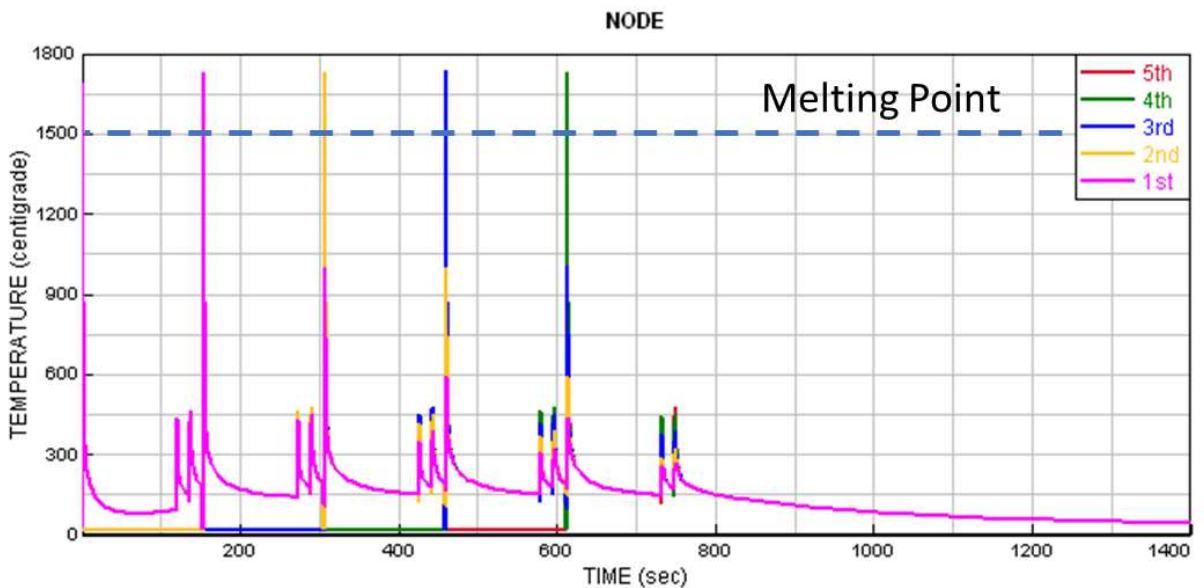


Figure 28. The thermal cycle of middle nodes on top of each layers in five-layer deposition scenario

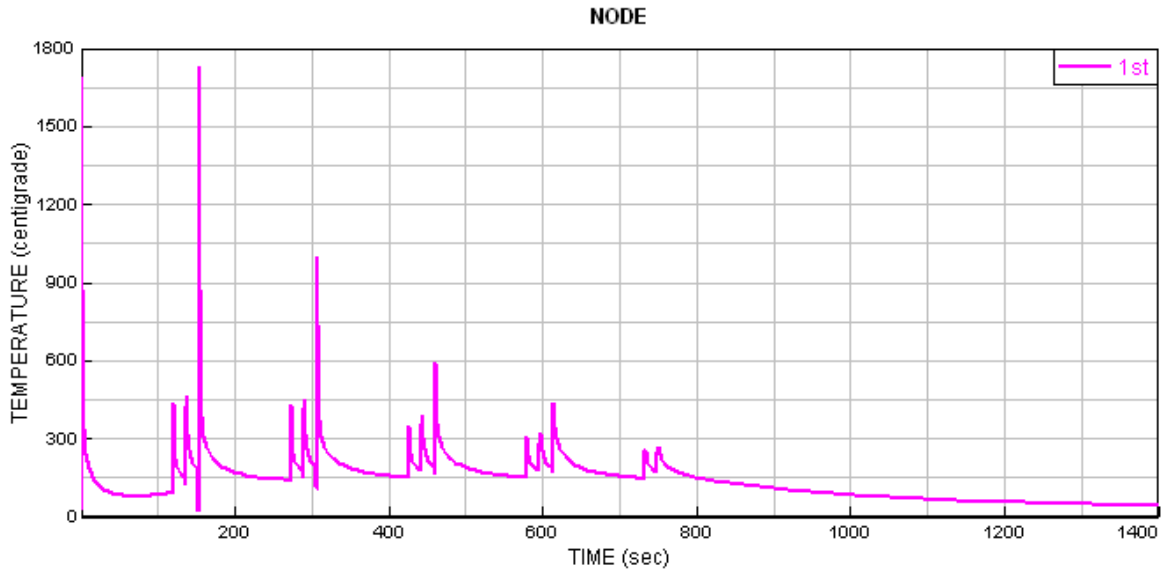


Figure 29. The thermal cycle of middle node on top of first layer in five-layer deposition scenario

In 3+2 layers scenario as shown in Figure 30, the first three layers are being preheated for 20 s to 100 °C and immediately the 4th and 5th layers are deposited. As shown if Figure 31 the third layer is exposed to a great thermal gradient and the temperature of the middle node on top of the 3rd layer increases sharply to above melting temperature while the 4th layer is being deposited. As a result, the sharp transition of stress result between the 3rd and the 4th layer can be due to the sharp temperature changes in the 3rd layer.

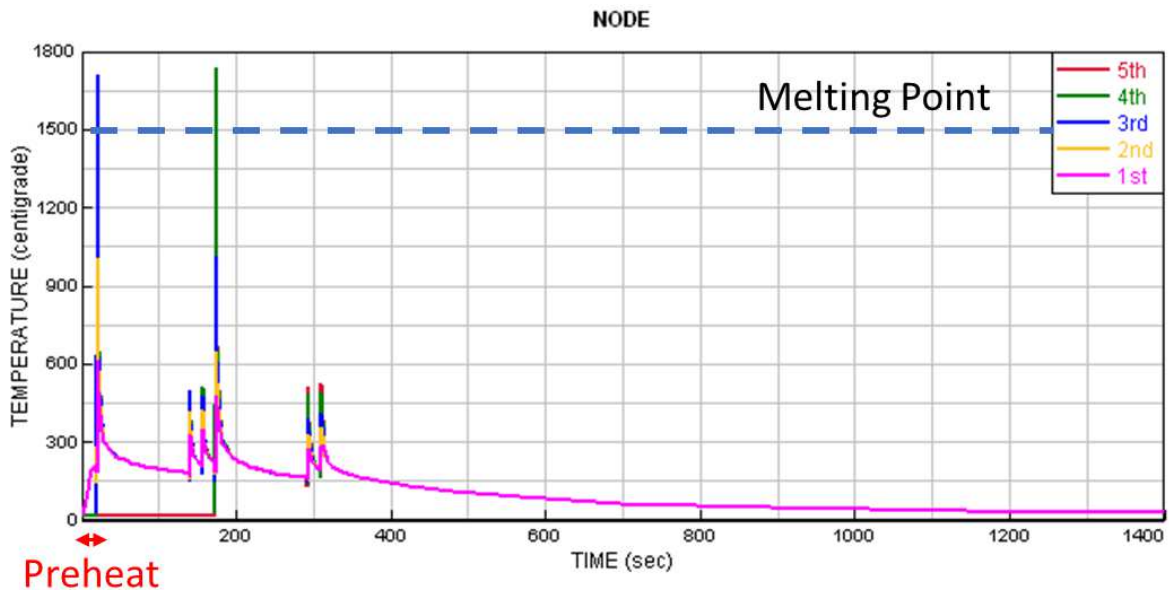


Figure 30. The thermal cycle of middle nodes on top of each layers in 3+2 layer deposition scenario

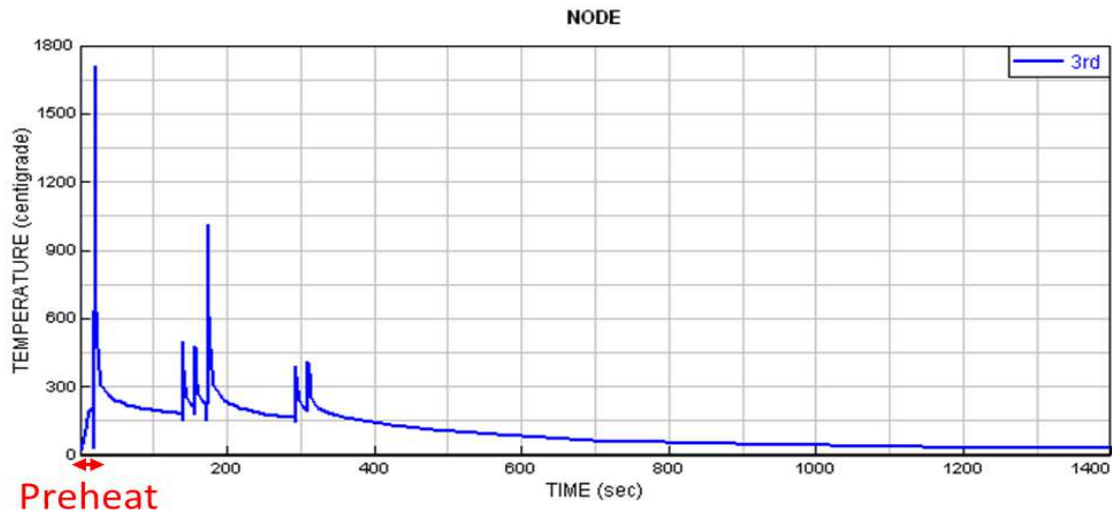


Figure 31. The thermal cycle of middle node on top of 3rd layer in 3+2 layer deposition scenario

As a result of this research, cladding for worn thin wall components, such as a roll die, will introduce unique residual stress build ups that will need to be managed for repair activities, and this preheat strategy is not a viable approach to reducing computational time.

Summary and conclusion

In this study, a thermo-metallurgical mechanical FE model was established to study the residual stress for a multi-joint component when using the laser cladding based DED AM process. The single and multi-layer thin-walled case studies, with junction structures, were modeled using the SYSWELD software package. The effect of the path strategy on the residual stress for different build strategies was explored, and distinct residual stress patterns were generated. A rigorous assessment of the resulting stress patterns was conducted, and the tool path that provided the least stress (Hex 3) was used for the subsequent analyses.

The application of an optimized method to reduce the computational time was proposed and tested. The optimized simulation technique was leveraged to explore the residual stress formation for the multi-layer thin-walled case studies. The major conclusions are as follows:

- Investigating different path strategies to determine an optimal deposition approach is an important research question. The three different path strategies for the one-layer thin wall hexagon scenario showed that the Hex 3 deposition path has the least amount of longitudinal, transverse and normal residual stress and lower overall maximum stresses as compared to the other path strategies. The effect of the tool path cannot be ignored and developing strategies to explore deposition options is an important area of research.
- The imposed thermal cycle approach can produce meaningful results with significantly less computational time. Consequently, it is an appropriate approach to investigate multilayer and more complex components which are difficult or impossible to study when using the transient method. This is critical when considering that the DED process lends itself thin walled components.

- The preheating of the primary layers cannot be a substitute for the deposition modeling approach. The thermal cycles being experienced by each deposited layer during the laser cladding process affects the thermal, metallurgical mechanical characteristics of the deposited layers and cannot be simplified by a preheating process. This virtual experiment highlighted a challenge to be addressed for the repair of thin wall components.

Knowledge obtained from these case studies provides a foundation for efficient and rapid optimization of laser cladding processes, with the aim of minimizing residual stress in both simple and complex laser cladding structures. Research to optimize joint designs, and interweave heat only passes or machining operations is future work along with considering the tool path direction and sequences.

Acknowledgements: This research is funded by the NSERC Discovery Grant. The authors gratefully acknowledge that.

Author contributions: Bita Mohajernia has done the data collection, analysis and writing. Dr. Jill Urbanic has contributed in writing and data analysis.

Funding This research is funded by the NSERC Discovery Grant.

Availability of data and material Not applicable.

Code availability Not applicable.

Declarations

Ethics approval The authors declare that this is an original work by them and the data used from previously published publications is cited in the paper. No data, text, or theories by others are presented as if they were the authors' own ("plagiarism"). The paper is not currently being considered for publication elsewhere.

Consent to participate Not applicable.

Consent for publication All authors approve the manuscript and give their consent for submission and publication in The International Journal of Advanced Manufacturing Technology.

Conflict of interest The authors declare no conflict of interests

References

- [1] W. Chen, L. Xu, Y. Han, L. Zhao, and H. Jing, "Control of residual stress in metal additive manufacturing by low-temperature solid-state phase transformation: An experimental and numerical study," *Additive Manufacturing*, vol. 42, p. 102016, Jun. 2021, doi: 10.1016/J.ADDMA.2021.102016.
- [2] M. Strantza *et al.*, "Directional and oscillating residual stress on the mesoscale in additively manufactured Ti-6Al-4V," *Acta Materialia*, vol. 168, pp. 299–308, Apr. 2019, doi: 10.1016/J.ACTAMAT.2019.01.050.
- [3] J. Zhang, X. Wang, S. Paddea, and X. Zhang, "Fatigue crack propagation behaviour in wire+arc additive manufactured Ti-6Al-4V: Effects of microstructure and residual stress," *Materials & Design*, vol. 90, pp. 551–561, Jan. 2016, doi: 10.1016/J.MATDES.2015.10.141.
- [4] J. C. Snyder, C. K. Stimpson, K. A. Thole, and D. Mongillo, "Build direction effects on additively manufactured channels," *Journal of Turbomachinery*, vol. 138, no. 5, p. 51006, 2016.

- [5] R. Li and J. Xiong, "A numerical prediction of residual stress for a thin-walled part with geometrical features fabricated by GMA-based additive manufacturing", doi: 10.1108/RPJ-08-2018-0193.
- [6] R. Li, J. Xiong, and Y. Lei, "Investigation on thermal stress evolution induced by wire and arc additive manufacturing for circular thin-walled parts," *Journal of Manufacturing Processes*, vol. 40, pp. 59–67, Apr. 2019, doi: 10.1016/J.JMAPRO.2019.03.006.
- [7] J. Xiong, Y. Lei, and R. Li, "Finite element analysis and experimental validation of thermal behavior for thin-walled parts in GMAW-based additive manufacturing with various substrate preheating temperatures," *Applied Thermal Engineering*, vol. 126, pp. 43–52, Nov. 2017, doi: 10.1016/J.APPLTHERMALENG.2017.07.168.
- [8] J. Xiong, R. Li, Y. Lei, and H. Chen, "Heat propagation of circular thin-walled parts fabricated in additive manufacturing using gas metal arc welding," *Journal of Materials Processing Technology*, vol. 251, pp. 12–19, Jan. 2018, doi: 10.1016/J.JMATPROTEC.2017.08.007.
- [9] H. Zhao, G. Zhang, Z. Yin, and L. Wu, "Three-dimensional finite element analysis of thermal stress in single-pass multi-layer weld-based rapid prototyping," *Journal of Materials Processing Technology*, vol. 212, no. 1, pp. 276–285, Jan. 2012, doi: 10.1016/J.JMATPROTEC.2011.09.012.
- [10] M. A. Somashekara, M. Naveenkumar, A. Kumar, C. Viswanath, and S. Simhambhatla, "Investigations into effect of weld-deposition pattern on residual stress evolution for metallic additive manufacturing," *The International Journal of Advanced Manufacturing Technology 2016 90:5*, vol. 90, no. 5, pp. 2009–2025, Oct. 2016, doi: 10.1007/S00170-016-9510-7.
- [11] Q. Wu, T. Mukherjee, C. Liu, J. Lu, and T. DebRoy, "Residual stresses and distortion in the patterned printing of titanium and nickel alloys," *Additive Manufacturing*, vol. 29, p. 100808, Oct. 2019, doi: 10.1016/J.ADDMA.2019.100808.
- [12] L. Sun, X. Ren, J. He, and Z. Zhang, "Numerical investigation of a novel pattern for reducing residual stress in metal additive manufacturing," *Journal of Materials Science & Technology*, vol. 67, pp. 11–22, Mar. 2021, doi: 10.1016/J.JMST.2020.05.080.
- [13] S. E. Mirazimzadeh, · Syamak Pazireh, J. Urbanic, and · Bob Hedrick, "Investigation of effects of different moving heat source scanning patterns on thermo-mechanical behavior in direct energy deposition manufacturing," *The International Journal of Advanced Manufacturing Technology*, doi: 10.1007/s00170-022-08970-2.
- [14] T. Kik and J. Górka, "materials Numerical Simulations of Laser and Hybrid S700MC T-Joint Welding," 2019, doi: 10.3390/ma12030516.
- [15] T. Kik, "materials Computational Techniques in Numerical Simulations of Arc and Laser Welding Processes", doi: 10.3390/ma13030608.
- [16] T. Kik, "Computational Techniques in Numerical Simulations of Arc and Laser Welding Processes," *Materials 2020, Vol. 13, Page 608*, vol. 13, no. 3, p. 608, Jan. 2020, doi: 10.3390/MA13030608.
- [17] "(7) (PDF) A computationally efficient finite element model of wire and arc additive manufacture | Alessandra Tesei - Academia.edu."

https://www.academia.edu/24320060/A_computationally_efficient_finite_element_model_of_wire_and_arc_additive_manufacture (accessed Mar. 01, 2022).

- [18] X. Pu, C. Zhang, S. Li, and D. Deng, "Simulating welding residual stress and deformation in a multi-pass butt-welded joint considering balance between computing time and prediction accuracy," *The International Journal of Advanced Manufacturing Technology* 2017 93:5, vol. 93, no. 5, pp. 2215–2226, Jun. 2017, doi: 10.1007/S00170-017-0691-5.
- [19] N. Nazemi and R. J. Urbanic, "A numerical investigation for alternative toolpath deposition solutions for surface cladding of stainless steel P420 powder on AISI 1018 steel substrate," *International Journal of Advanced Manufacturing Technology*, vol. 96, no. 9–12, pp. 4123–4143, Jun. 2018, doi: 10.1007/S00170-018-1840-1.
- [20] M. Zhu, Y. Zhang, Q. Zheng, W. Wu, W. Qian, and B. Wang, "Influence of Welding Sequence on Residual Stress Evolution in SUS304/Q235 Bimetallic Clad Plate Butt-Welded Joints," *asmedigitalcollection.asme.org*, 2021, Accessed: Feb. 28, 2022. [Online]. Available: <https://asmedigitalcollection.asme.org/IMECE/proceedings-abstract/IMECE2021/V003T03A016/1132539>
- [21] X. Wang, E. G.-F. ed I. Strutturale, and undefined 2020, "Numerical analysis and verification of residual stress in T joint of S355 steel," *78.47.113.247*, vol. 52, pp. 25–32, 2020, doi: 10.3221/IGF-ESIS.52.03.
- [22] X. Lu *et al.*, "Residual stress and distortion of rectangular and S-shaped Ti-6Al-4V parts by Directed Energy Deposition: Modelling and experimental calibration," *Additive Manufacturing*, vol. 26, pp. 166–179, Mar. 2019, doi: 10.1016/J.ADDMA.2019.02.001.
- [23] T. Kik, "Computational Techniques in Numerical Simulations," 2020.
- [24] N. Nazemi, J. Urbanic, and M. Alam, "Hardness and residual stress modeling of powder injection laser cladding of P420 coating on AISI 1018 substrate", doi: 10.1007/s00170-017-0760-9.
- [25] T. Kik, J. Górka, A. Kotarska, and T. Poloczek, "Numerical verification of tests on the influence of the imposed thermal cycles on the structure and properties of the S700MC heat-affected zone," *Metals (Basel)*, vol. 10, no. 7, pp. 1–23, 2020, doi: 10.3390/met10070974.
- [26] S. Gauthier, S. I. Abarzhi, K. R. Sreenivasan, T. Kik, J. Moravec, and I. Novakova, "New method of processing heat treatment experiments with numerical simulation support," *IOP Conference Series: Materials Science and Engineering*, vol. 227, no. 1, p. 012069, Aug. 2017, doi: 10.1088/1757-899X/227/1/012069.
- [27] R. Li *et al.*, "Effect of path strategy on residual stress and distortion in laser and cold metal transfer hybrid additive manufacturing," *Additive Manufacturing*, vol. 46, no. June, p. 102203, 2021, doi: 10.1016/j.addma.2021.102203.
- [28] D. Deng and H. Murakawa, "Numerical simulation of temperature field and residual stress in multi-pass welds in stainless steel pipe and comparison with experimental measurements," *Computational Materials Science*, vol. 37, no. 3, pp. 269–277, Sep. 2006, doi: 10.1016/J.COMMATSCI.2005.07.007.

- [29] J. Xiong, Y. Lei, and R. Li, "Finite element analysis and experimental validation of thermal behavior for thin-walled parts in GMAW-based additive manufacturing with various substrate preheating temperatures," *Applied Thermal Engineering*, vol. 126, pp. 43–52, Nov. 2017, doi: 10.1016/J.APPLTHERMALENG.2017.07.168.
- [30] J. Xiong, R. Li, Y. Lei, and H. Chen, "Heat propagation of circular thin-walled parts fabricated in additive manufacturing using gas metal arc welding," *Journal of Materials Processing Technology*, vol. 251, pp. 12–19, Jan. 2018, doi: 10.1016/J.JMATPROTEC.2017.08.007.
- [31] S. Jayanath and A. Achuthan, "A Computationally Efficient Finite Element Framework to Simulate Additive Manufacturing Processes," *Journal of Manufacturing Science and Engineering, Transactions of the ASME*, vol. 140, no. 4, Apr. 2018, doi: 10.1115/1.4039092/380516.
- [32] N. Hoyer, H. J. Li, D. Cuiuri, and A. Paradowska, "Measurement of Residual Stresses in Titanium Aerospace Components Formed via Additive Manufacturing," *Materials Science Forum*, vol. 777, pp. 124–129, 2014, doi: 10.4028/WWW.SCIENTIFIC.NET/MSF.777.124.
- [33] R. J. Urbanic, B. Mohajernia, and N. Nazemi, "Developing geometric analysis tools to compare heat map results for metal additive manufactured components," *Comput Aided Des Appl*, vol. 17, no. 2, pp. 288–311, 2019.